AFRL-RV-PS-
TR-2022-0099

AFRL-RV-PS-
TR-2022-0090

AFRL-RV-PS-
TR-2022-0099

ON-ORBIT ESTIMATION OF SPACECRAFT MASS PROPERTIES

Kyle J. DeMars and J. Cameron Helmuth

Texas A&M Engineering Experiment Station
1470 William D Fitch Pkwy
College Station, TX 77843-3577

30 September 2022

Final Report

AIR FORCE RESEARCH LABORATORY
Space Vehicles Directorate
3550 Aberdeen Ave SE
AIR FORCE MATERIEL COMMAND
KIRTLAND AIR FORCE BASE, NM 87117-5776

DTIC COPY

NOTICE AND SIGNATURE PAGE

AFRL-RV-PS-TR-2022-0099 HAS BEEN REVIEWED AND IS APPROVED FOR PUBLICATION IN ACCORDANCE WITH ASSIGNED DISTRIBUTION STATEMENT.

//SIGNED//	//SIGNED//
_____	_____
CAPT DAVID KING Program Manager	For: ANDREW SINCLAIR Tech Advisor, Space Component Technology Branch

REPORT DOCUMENTATION PAGE

Form Approved
OMB No. 0704-0188

1. REPORT DATE *(DD-MM-YYYY)*	**2. REPORT TYPE**	**3. DATES COVERED** *(From - To)*
30-Sep-2022	Final Report	20-May-2020 – 30-Sep-2022

4. TITLE AND SUBTITLE
On-Orbit Estimation of Spacecraft Mass Properties

5a. CONTRACT NUMBER
FA9453-20-1-0042

5b. GRANT NUMBER

5c. PROGRAM ELEMENT NUMBER
C6601F

6. AUTHOR(S)
Kyle J. DeMars and J. Cameron Helmuth

5d. PROJECT NUMBER
8809

5e. TASK NUMBER
EF133986

5f. WORK UNIT NUMBER
V1JM

7. PERFORMING ORGANIZATION NAME(S) AND ADDRESS(ES)
Texas A&M Engineering Experiment Station
1470 William D Fitch Pky
College Station, TX 77843-3577

8. PERFORMING ORGANIZATION REPORT NUMBER

9. SPONSORING / MONITORING AGENCY NAME(S) AND ADDRESS(ES)
Air Force Research Laboratory
Space Vehicles Directorate
3550 Aberdeen Avenue SE
Kirtland AFB, NM 87117-5776

10. SPONSOR/MONITOR'S ACRONYM(S)
AFRL/RVSV

11. SPONSOR/MONITOR'S REPORT NUMBER(S)
AFRL-RV-PS-TR-2022-0099

12. DISTRIBUTION / AVAILABILITY STATEMENT
Approved for public release; distribution is unlimited AFRL-2023-2050 dtd 28 Apr 2023.

13. SUPPLEMENTARY NOTES
On-Orbit Estimation of Spacecraft Mass Properties

14. ABSTRACT
Timely, accurate, and precise estimation of spacecraft mass properties, such as the inertia tensor, using onboard measurement data is key to enabling precision attitude control and understanding the configuration of a vehicle on-orbit. Estimating the inertia tensor, however, is complicated by the constraints required to produce a valid representation of the mass distribution. Effective estimation is also facilitated by appropriate control inputs, a topic that is elucidated through observability analysis. This work investigates observability analysis to optimize the observability of the inertia tensor and proposes, develops, and analyzes estimation approaches that satisfy the requisite inequality constraints of the inertia tensor.

15. SUBJECT TERMS
attitude determination; inertia tensor estimation; nonlinear observability; constrained estimation

16. SECURITY CLASSIFICATION OF:			**17. LIMITATION OF ABSTRACT**	**18. NUMBER OF PAGES**	**19a. NAME OF RESPONSIBLE PERSON**
					David King
a. REPORT	**b. ABSTRACT**	**c. THIS PAGE**	Unlimited	52	**19b. TELEPHONE NUMBER** *(include area code)*
Unclassified	Unclassified	Unclassified			

(This Page Intentionally Left Blank)

TABLE OF CONTENTS

Section **Page**

LIST OF FIGURES

Figure **Page**

LIST OF TABLES

Table **Page**

ACKNOWLEDGMENTS

This material is based on research sponsored by Air Force Research Laboratory under agreement number FA9453-20-1-0042. The U.S. Government is authorized to reproduce and distribute reprints for Governmental purposes notwithstanding any copyright notation thereon.

DISCLAIMER

The views and conclusions contained herein are those of the authors and should not be interpreted as necessarily representing the official policies or endorsements, either expressed or implied, of Air Force Research Laboratory or the U.S. Government.

1.0 SUMMARY

Timely, accurate, and precise estimation of spacecraft mass properties, such as the inertia tensor, using onboard measurement data is key to enabling precision attitude control and understanding the configuration of a vehicle on-orbit. Estimating the inertia tensor, however, is complicated by the constraints required to produce a valid representation of the mass distribution. Effective estimation is also facilitated by appropriate control inputs, a topic that is elucidated through observability analysis. This work investigates observability analysis to optimize the observability of the inertia tensor and proposes, develops, and analyzes estimation approaches that satisfy the requisite inequality constraints of the inertia tensor.

2.0 INTRODUCTION

Effective control of the attitude of a spacecraft requires knowledge of the parameters that define the attitude dynamics. If a spacecraft can be adequately modeled as a rigid body, the temporal evolution of the angular velocity is governed by Euler's equation, and the parameters that define the system are the inertia tensor—the symmetric 3×3 matrix that describes the mass distribution of the vehicle—and the actuator pose. While the actuator locations are usually known with high accuracy, this is not always the case for the inertia tensor. It may be possible to measure the inertia tensor prior to launch[1]; however, this task becomes increasingly challenging with larger spacecraft. If the inertia tensor cannot be measured before launch, operators must rely on computer-aided design (CAD) models of the spacecraft. In either situation, the inertia tensor is imperfectly known, which can result in degraded attitude control performance. To complicate the issue, even when a spacecraft can be accurately modeled as a rigid body, its inertia tensor will likely not be constant for the duration of the mission life. A variety of alterations to the spacecraft such as fuel expenditure, deployment of antennas or robotic arms, or crew movement all change the distribution of the vehicle's mass and, thus, its inertia tensor. Once again, CAD models can be used to approximate these changes, but such approximations may not be sufficiently accurate.

Inaccurate knowledge of the inertia tensor has a direct, deleterious effect on control performance, so it can be advantageous to estimate the inertia of the spacecraft on orbit. However, the inertia tensor must adhere to several constraints. As such, producing an estimate that satisfies the physical reality is a nontrivial problem. A number of approaches to onboard inertia estimation have been presented in literature [1–8], and, while these are effective solutions in many situations, there is still work to be done. Some of these approaches utilize the measurement noise statistics to generate estimates with some associated measure of uncertainty, and others produce estimates that are guaranteed to satisfy the physical constraints, but a statistical estimation approach that satisfies state constraints and provides a measure of the estimate uncertainty is lacking. Previous work has also investigated the effect of the parameters chosen to represent the inertia tensor on estimation performance, demonstrating that a proper selection of parameters can affect the complexity of enforcing state constraints, even eliminating some constraints [9].

Due to the nonlinear dynamics that govern spacecraft attitude evolution, observation and control are coupled problems. As such, the chosen control signal influences the degree to which the system states can be observed, and, therefore, it is possible to determine slewing maneuvers that optimize the observability of the spacecraft inertia tensor. For nonlinear systems, observability can be complicated to discuss, since, in general, it is impossible to check for global observability. Common approaches leverage the linearized observability Gramian to investigate observability in this system

[1] `https://www.space-electronics.com/contentAssets/Literature/Space%20Electronics%20Mass%20Properties%20Laboratory%20Measurement%20Services.pdf`

[10, 11]. Other work in observability optimization has made use of the empirical observability Gramian [12] for its advantages in accuracy over direct computation of the linearized observability Gramian with relative ease of computation. In Ref. 13, the Kalman filter covariance matrix is used as the measure of observability in order to find suboptimal orbit transfers (in terms of fuel expenditure) that improve system observability. This report discusses both linearized and nonlinear observability Gramians, where the nonlinear observability Gramian is constructed from the gradient of the Lie derivatives of the observations with respect to the dynamics [14, 15].

In the pursuit of estimation approaches that have potential for onboard implementation, this report develops recursive filtering approaches to inertia tensor estimation. Perhaps the most frequently chosen method for recursive estimation is the extended Kalman filter (EKF) [16]. For linear systems with white process and measurement noise, the Kalman filter is the linear estimator that minimizes the mean squared error [17]. The EKF applies the Kalman filter framework to nonlinear systems by linearizing them about the current estimate. The modification to the EKF for attitude estimation is the multiplicative EKF (MEKF) [18]; it is ubiquitous in many attitude estimation applications. Several approaches have been developed to incorporate linear state equality constraints into the Kalman filter framework. Ref. 19 showed that such constraints can be processed in the filter as perfect measurements, i.e., functions of the state vector with no corrupting noise. While this approach theoretically yields the constrained estimate, processing noise-free measurements leads to a singular covariance matrix in practice. Inequality constraints can also be considered as part of the underlying optimization problem. Solutions to the equality constrained least squares problem are presented in Ref. 20, and Ref. 21 shows that the constrained estimate can be acquired by projecting the unconstrained estimate onto the constraint surface. Work has also been done to address the more complex situation of enforcing state inequality constraints. Ref. 22 presents a solution to the least squares problem with linear inequality constraints by converting it into a least distance programming problem. Another solution presented in Ref. 23 is to extend the projection approach for linear equality constraints from Ref. 21 to linear inequality constraints by formulating the problem as a quadratic programming problem. This report discusses the constrained estimation problem by reformulating the linear, minimum mean-square error framework as an constrained optimization problem and by investigating Bayesian approaches that can be amended to handle constraints in a straightforward manner.

The remainder of this report is organized as follows. Section 3.1 provides an overview of the modeling considerations required for both unactuated and reaction-wheel-actuated rigid bodies, as well as a discussion on the inertia tensor and the measurement models used in this work. Section 3.2 develops linearized and nonlinear observability analysis techniques and includes discussions about numerical considerations. The theory and development of various estimation approaches that are capable of handling inertia tensor constraints are presented in Section 3.3. Linearized observability analysis results are presented and discussed in Section 4.1 for a variety of different control input signals. Section 4.2, on the other hand, demonstrates how to use nonlinear observability analysis to optimize control input signals. Section 4.3 provides an analysis of the application of the developed estimation approaches for the estimation of the inertia tensor under different levels of initial uncertainty. Section 5.0 concludes the report with recommendations as to how the presented methods can be used in practice.

3.0 METHODS, ASSUMPTIONS, AND PROCEDURES

3.1 Dynamics and Measurements

3.1.1 Attitude Representation and Kinematics

A variety of parameterizations have been invented to quantify the attitude of a vehicle [24, 25]. Some of the more common approaches include the direction cosine matrix (DCM), Euler angle sequences, and the attitude quaternion. The attitude quaternion, denoted by $\bar{\boldsymbol{q}}$, is especially attractive, as it is a four parameter, globally nonsingular set of attitude coordinates. However, since attitude in three dimensions only has three degrees of freedom, the quaternion is constrained to the unit hypersphere according to $\|\bar{\boldsymbol{q}}\| = 1$. Furthermore, the attitude quaternion is a two-to-one representation, such that $\pm\bar{\boldsymbol{q}}$ represent identical attitudes. These properties must be accounted for when using a quaternion to represent vehicle attitude; however, out of the globally nonsingular attitude representations, these properties are generally the most straightforward to enforce. As such, the attitude quaternion is chosen to represent attitude in the dynamical system considered.

The attitude quaternion is defined to have its "vector" part first, according to

$$\bar{\boldsymbol{q}} = \begin{bmatrix} \boldsymbol{q} \\ q \end{bmatrix}, \tag{1}$$

where $\boldsymbol{q}$ and q are the vector and scalar parts of the quaternion, respectively. Within this work, there are three coordinate systems of interest. The inertial coordinate system is denoted by i; a coordinate system affixed to the "vehicle" is denoted by b; and a principal axis coordinate system, which will be discussed further in Section 3.1.4, is denoted by p. When representing multiple attitudes, it is necessary to specify coordinate systems. To that end, $\bar{\boldsymbol{q}}_i^b$ represents the attitude of the body-fixed coordinate system with respect to the inertial coordinate system, and $\bar{\boldsymbol{q}}_p^b$ represents the attitude of the body-fixed coordinate system with respect to the principal axis coordinate system. When there is no potential for ambiguity, the sub- and superscripts are omitted for notational simplicity.

Letting $\bar{\boldsymbol{q}}$ denote the attitude of the body axes with respect to the inertial axes, the kinematics defining the temporal evolution of the attitude quaternion are given by [25]

$$\dot{\bar{\boldsymbol{q}}} = \frac{1}{2}\bar{\boldsymbol{\omega}} \otimes \bar{\boldsymbol{q}}\,, \tag{2}$$

where $\bar{\boldsymbol{\omega}} = [\boldsymbol{\omega}^T \;\; 0]^T$ is the pure quaternion form of $\boldsymbol{\omega}$, which is in turn the angular velocity of the vehicle body axes with respect to the inertial coordinate system expressed in the body axes. The "$\otimes$" operator represents quaternion multiplication, which is given by

$$\bar{\boldsymbol{q}} \otimes \bar{\boldsymbol{p}} = \begin{bmatrix} p\boldsymbol{q} + q\boldsymbol{p} - \boldsymbol{q} \times \boldsymbol{p} \\ qp - \boldsymbol{q} \cdot \boldsymbol{p} \end{bmatrix} = \begin{bmatrix} q\boldsymbol{I}_3 - [\boldsymbol{q}\times] & \boldsymbol{q} \\ -\boldsymbol{q}^T & q \end{bmatrix} \boldsymbol{p}\,, \tag{3}$$

where $\boldsymbol{I}_n$ denotes a n-dimensional identity matrix,

$$\bar{\boldsymbol{p}} = \begin{bmatrix} \boldsymbol{p} \\ p \end{bmatrix} \tag{4}$$

is an arbitrary quaternion, and

$$[\boldsymbol{a}\times] = \begin{bmatrix} 0 & -a_3 & a_2 \\ a_3 & 0 & -a_1 \\ -a_2 & a_1 & 0 \end{bmatrix}, \tag{5}$$

for any vector $\boldsymbol{a} = [a_1 \;\; a_2 \;\; a_3]^T \in \mathbb{R}^3$. The opposite rotation of the rotation corresponding to $\bar{\boldsymbol{q}}$ is given by its inverse, which is defined for attitude quaternions according to

$$\bar{\boldsymbol{q}}^{-1} = \begin{bmatrix} -\boldsymbol{q} \\ q \end{bmatrix} . \tag{6}$$

It is sometimes required to find the equivalent DCM corresponding to a quaternion representation of attitude. The mapping of the quaternion to the DCM is given by [25]

$$\boldsymbol{T}(\bar{\boldsymbol{q}}) = \frac{1}{\bar{\boldsymbol{q}}^T\bar{\boldsymbol{q}}}\left[(q^2 - \boldsymbol{q}^T\boldsymbol{q})\boldsymbol{I}_3 - 2q[\boldsymbol{q}\times] + 2\boldsymbol{q}\boldsymbol{q}^T\right], \tag{7}$$

where $\boldsymbol{q}$ indicates the vector part of the quaternion and q denotes the scalar part. It should be noted that attitude quaternions always have a norm of 1, since they reside on the unit hypersphere; however, if one wishes to treat them as unconstrained vectors, the coefficient $(1/\bar{\boldsymbol{q}}^T\bar{\boldsymbol{q}})$ in Eq. (7) is necessary to ensure a proper orthogonal DCM. Notationally, if $\bar{\boldsymbol{q}}_a^b$ represents the attitude of coordinate system b with respect to coordinate system a in terms of the quaternion, the application of Eq. (7) produces $\boldsymbol{T}_a^b$, which is the DCM representation of the attitude of coordinate system b with respect to coordinate system a.

3.1.2 Rigid Body Dynamics

In many cases, a spacecraft can be approximated as a unactuated rigid body, such that the temporal evolution of the angular velocity is given by Euler's equation [25],

$$\dot{\boldsymbol{\omega}} = \boldsymbol{J}^{-1}[\boldsymbol{\tau}_{\text{ext}} - \boldsymbol{\omega}\times\boldsymbol{J}\boldsymbol{\omega}], \tag{8}$$

where $\boldsymbol{\omega}$ is the angular velocity vector of the spacecraft body axes with respect to the inertial frame, $\boldsymbol{J}$ is the inertia tensor with respect to the center of mass, and $\boldsymbol{\tau}_{\text{ext}}$ is the net external torque acting on the body. While Eq. (8) is expressed without coordinate system designations, it is herein assumed that all elements are coordinated in the body axes. That is to say that the inertia tensor, the angular velocity vector, and the torque vector are all expressed in coordinate system b.

3.1.3 Actuated Dynamics

Under the influence of reaction wheels and an external torque, the temporal evolution of the angular velocity is given by combining Eqs. 3.145, 3.146, and 3.147 in Ref. 25 and solving for $\dot{\boldsymbol{\omega}}$ to yield

$$\dot{\boldsymbol{\omega}} = \left[\boldsymbol{J} + \sum_{\ell=1}^{n_w} J_\ell^{\parallel}\,\boldsymbol{n}_\ell^{\parallel}\,(\boldsymbol{n}_\ell^{\parallel})^T\right]^{-1}\left[\boldsymbol{\tau}_{\text{ext}} - \sum_{\ell=1}^{n_w} J_\ell^{\parallel}\,\dot{\omega}_\ell\,\boldsymbol{n}_\ell^{\parallel} - \boldsymbol{\omega}\times(\boldsymbol{J}\boldsymbol{\omega} + \boldsymbol{h}_w)\right], \tag{9}$$

where $\boldsymbol{J}$ is the inertia tensor of the vehicle with respect to its center of mass, coordinated in the body axes. This inertia tensor includes the transverse moments of inertia (the moments of inertia normal to the spin axis) of the reaction wheels, and $J_\ell^{\parallel}$ is the moment of inertia about the spin axis of the ℓ^{th} reaction wheel. The unit vector defining the spin axis of the ℓ^{th} reaction wheel is $\boldsymbol{n}_\ell^{\parallel}$, $\dot{\omega}_\ell^{\parallel}$ is the known commanded acceleration of the ℓ^{th} reaction wheel, $\boldsymbol{\tau}_{\text{ext}}$ is the external torque acting on the vehicle expressed in the body frame, n_w is the number of reaction wheels on the vehicle, $\boldsymbol{h}_w$, which is given by

$$\boldsymbol{h}_w = \sum_{\ell=1}^{n_w} J_\ell^{\parallel}(\boldsymbol{n}_\ell^{\parallel}\cdot\boldsymbol{\omega} + \omega_\ell)\boldsymbol{n}_\ell^{\parallel}, \tag{10}$$

is the total angular momentum of the reaction wheels expressed in the body frame, and ω_ℓ is the angular speed of the ℓ^{th} reaction wheel.

3.1.4 Inertia Tensor

Spacecraft attitude dynamics, as defined by Eq. (8) or Eq. (9), depend on the inertia tensor, $\boldsymbol{J}$. The inertia tensor is a real, symmetric, positive-definite 3×3 matrix. In the most general case, the inertia tensor takes the form

$$\boldsymbol{J} = \begin{bmatrix} j_{xx} & j_{xy} & j_{xz} \\ j_{xy} & j_{yy} & j_{yz} \\ j_{xz} & j_{yz} & j_{zz} \end{bmatrix} , \tag{11}$$

where the diagonal elements of $\boldsymbol{J}$ are referred to as the moments of inertia, and the off-diagonal elements are referred to as the products of inertia. The numerical value that each entry in $\boldsymbol{J}$ takes on depends on the basis vectors in which the tensor is coordinated, e.g., the vehicle body axes or a set of so-called principal axes. An inertia tensor coordinated in the body axes can be decomposed into a set of principal axes through spectral decomposition,

$$\boldsymbol{J}^b = \boldsymbol{T}_p^b \boldsymbol{J}^p (\boldsymbol{T}_p^b)^T = \boldsymbol{T}_p^b \begin{bmatrix} j_{xx}^p & 0 & 0 \\ 0 & j_{yy}^p & 0 \\ 0 & 0 & j_{zz}^p \end{bmatrix} (\boldsymbol{T}_p^b)^T , \tag{12}$$

where $\boldsymbol{J}^b$ is the inertia tensor expressed in a body-fixed coordinate system, $\boldsymbol{J}^p$ is the inertia tensor expressed in the principal axis coordinate system, and $\boldsymbol{T}_p^b$ is the DCM that maps from the principal axes to the body axes. Besides symmetry and positivity, every inertia tensor must also adhere to the constraints

$$j_{aa} \leq j_{bb} + j_{cc} \tag{13a}$$

$$j_{ab}^2 \leq j_{aa} j_{bb} \tag{13b}$$

$$j_{aa} \geq 2|j_{bc}| , \tag{13c}$$

where the indices $a,\ b,\ c$ are any permutation of the set $\{x,\ y,\ z\}$ [26]. Equation (13a) states that any moment of inertia must be no greater than the sum of the other two moments. It is referred to as the triangle inequality, since the sides of a triangle also adhere to this constraint. Equation (13b) states that the square of each product of inertia must be less than or equal to the product of the two corresponding moments; because of the quadratic form it is referred to as the quadratic inequality. Equation (13c) indicates that the moments of inertia have much larger magnitude than the products, so this is referred to as the diagonal dominance inequality.

The objective of this report is to investigate the estimation of mass properties of an on-orbit vehicle or spacecraft; specifically, the focus is on the estimation of the inertia tensor of the vehicle. When attempting to estimate the inertia tensor, a set of parameters must be chosen to define the inertia tensor, and, in order to guarantee an estimate that is physically possible, the constraints must be enforced somehow in the estimator. One common choice of parameters is the six unique entries in $\boldsymbol{J}^b$: j_{xx}^b, j_{yy}^b, j_{zz}^b, j_{xy}^b, j_{xz}^b, and j_{yz}^b—the body moments and products of inertia. This choice of parameters leaves to the estimator the job of ensuring that the resultant inertia tensor estimate is positive definite and adheres to all of the constraints in Eqs. (13). Alternatively, the inertia tensor can be parameterized, as in Eq. (12), by the principal moments of inertia (j_{xx}^p, j_{yy}^p, and j_{zz}^p) and a representation of the attitude of the principal axes, i.e., $\bar{\boldsymbol{q}}_p^b$. In this case, the inertia tensor estimate is positive definite if

$$j_{aa}^p > 0 \ \ \forall\ a \in \{x, y, z\} , \tag{14}$$

and, if Eq. (14) is satisfied, Eqs. (13b) and (13c) are also satisfied. The estimator then only needs to satisfy Eq. (13a) and Eq. (14)—six linear inequality constraints—and to produce a valid estimate of the attitude, $\boldsymbol{T}_p^b$, which can be accomplished by estimating the equivalent quaternion, $\bar{\boldsymbol{q}}_p^b$, which must satisfy a unit-norm constraint.

3.1.5 System States

The elements of the inertia tensor cannot be directly measured for an object in orbit. As such, it is necessary to estimate the parameters that define the inertia tensor by correlating them to quantities that can be directly measured. Given the preferential constraint structure of the principal moments and attitude of the principal axis coordinate system, the parameters selected to represent the inertia tensor are given by the principal moments of inertia, $\boldsymbol{j}_m^p = [j_{xx}^p \;\; j_{yy}^p \;\; j_{zz}^p]^T$ and the four elements of the quaternion $\bar{\boldsymbol{q}}_p^b$.

From Eq. (8) or Eq. (9), it is clear that the inertia tensor influences the dynamics of the vehicle. As such, if the angular velocity vector of the body-fixed coordinate system with respect to the inertial coordinate system can be measured, then it is possible to gain insight into the values that comprise the inertia tensor. Therefore, one potential set of coupled parameters to leverage in an estimator is given by

$$\boldsymbol{x} = \begin{bmatrix} \boldsymbol{\omega}^T & (\boldsymbol{j}_m^p)^T & (\bar{\boldsymbol{q}}_p^b)^T \end{bmatrix}^T , \tag{15}$$

which has temporal evolution

$$\dot{\boldsymbol{x}} = \boldsymbol{f}(\boldsymbol{x}, \boldsymbol{u}) = \begin{bmatrix} \dot{\boldsymbol{\omega}}^T & \boldsymbol{0}_3^T & \boldsymbol{0}_4^T \end{bmatrix}^T , \tag{16}$$

where $\boldsymbol{0}_n$ is an n-dimensional column array of zeros, $\dot{\boldsymbol{\omega}}$ is given by Eq. (8) or Eq. (9), and the control vector, $\boldsymbol{u}$, is taken to be the external torque, $\boldsymbol{\tau}_{\text{ext}}$, concatenated with the commanded angular acceleration of the n_w reaction wheels, $\dot{\omega}_\ell$, if appropriate. The vehicle controls are assumed to be perfectly commanded.

Observations of the angular velocity vector are typically obtained via a triad of single-axis gyroscopes as part of the inertial measurement unit (IMU) onboard the vehicle. These sensors are commonly affected by sensing errors, where the most dominant effect is that of bias. In such cases, it may be desirable to also estimate the gyro bias, $\boldsymbol{b}_g$. Doing so, however, requires additional measurements in order to separate out biases via independent data. The common inclusion for onboard operations is to leverage a star tracker, which provides information on the inertial attitude of the vehicle, $\bar{\boldsymbol{q}}_i^b$ or simply $\bar{\boldsymbol{q}}$. This combination gives rise to another set of coupled parameters to leverage in the estimator, which is

$$\boldsymbol{x} = \begin{bmatrix} \bar{\boldsymbol{q}}^T & \boldsymbol{\omega}^T & \boldsymbol{b}_g^T & (\boldsymbol{j}_m^p)^T & (\bar{\boldsymbol{q}}_p^b)^T \end{bmatrix}^T , \tag{17}$$

which, under the assumption of a random, constant gyro bias, has temporal evolution

$$\dot{\boldsymbol{x}} = \boldsymbol{f}(\boldsymbol{x}, \boldsymbol{u}) = \begin{bmatrix} \dot{\bar{\boldsymbol{q}}}^T & \dot{\boldsymbol{\omega}}^T & \boldsymbol{0}_3^T & \boldsymbol{0}_3^T & \boldsymbol{0}_4^T \end{bmatrix}^T , \tag{18}$$

where $\dot{\bar{\boldsymbol{q}}}$ is given by Eq. (2), $\dot{\boldsymbol{\omega}}$ is given by Eq. (8) or Eq. (9), and the control vector, $\boldsymbol{u}$, is taken to be the external torque, $\boldsymbol{\tau}_{\text{ext}}$, concatenated with the commanded angular acceleration of the n_w reaction wheels, $\dot{\omega}_\ell$, if appropriate. The vehicle controls are assumed to be perfectly commanded.

In either selection of the system states, the corresponding dynamics are of the form

$$\dot{\boldsymbol{x}}(t) = \boldsymbol{f}(\boldsymbol{x}(t), \boldsymbol{u}(t), \boldsymbol{w}(t)) , \tag{19}$$

where $\boldsymbol{x}(t)$ is the time-varying state of the system, $\boldsymbol{u}(t)$ is the time-varying input to the system, and $\boldsymbol{w}(t)$ is the time-varying process noise in the system. As cast, the kinematics of Eq. (2) and the dynamics of Eq. (8) or Eq. (9) do not contain any process noise elements; nevertheless, inclusion of process noise can be considered as a generalization of the presented models.

3.1.6 Measurements

To accompany the dynamics, measurements of the states are modeled as

$$\boldsymbol{z}_k = \boldsymbol{h}(\boldsymbol{x}_k, \boldsymbol{v}_k)\,, \tag{20}$$

where the subscript k denotes an instance in time, t_k, $\boldsymbol{z}_k$ is the measurement acquired at t_k, $\boldsymbol{x}_k$ is the corresponding state of the system at t_k, and $\boldsymbol{v}_k$ is the measurement noise. Given the discussion of Section 3.1.5, two sensor systems are considered in this work: a set of body-fixed gyrosopes and a star tracker.

3.1.6.1 Gyroscope

Most spacecraft are equipped with a set of three gyroscopes arranged in an orthogonal triad capable of measuring the angular velocity of the vehicle at a very high rate. The measured angular velocity is modeled as

$$\boldsymbol{\omega}_{m,k} = \boldsymbol{\omega}_k + \boldsymbol{b}_g + \boldsymbol{v}_{g,k}\,, \tag{21}$$

where the subscript k indicates the measurement epoch, $\boldsymbol{\omega}_{m,k}$ is the measured angular velocity at t_k, $\boldsymbol{\omega}_k$ is the true angular velocity of the body-fixed coordinate system with respect to ther inertial coordinate system at t_k, $\boldsymbol{b}_g$ is a random constant bias, and $\boldsymbol{v}_{g,k}$ is measurement noise that is modeled as a Gaussian random vector with zero mean and covariance

$$\boldsymbol{P}_{vv,g} = \sigma_g^2 \boldsymbol{I}_3\,, \tag{22}$$

where $\boldsymbol{I}_n$ denotes the $n \times n$ identity matrix. The gyro bias is initially sampled from a Gaussian distribution with zero mean and covariance

$$\boldsymbol{P}_{bb,g} = \sigma_b^2 \boldsymbol{I}_3\,. \tag{23}$$

3.1.6.2 Star Tracker

Many spacecraft that have precise attitude requirements are equipped with star trackers. These sensors use a camera to match images of stars with a catalog to produce a "measurement" of an attitude quaternion. This measurement is modeled as

$$\bar{\boldsymbol{q}}_{m,k} \propto \begin{bmatrix} \frac{1}{2}\boldsymbol{v}_{st,k} \\ 1 \end{bmatrix} \otimes \bar{\boldsymbol{q}}_k\,, \tag{24}$$

where $\bar{\boldsymbol{q}}_{m,k}$ is the measured quaternion of the inertial-to-body attitude, $\bar{\boldsymbol{q}}_k$ is the true quaternion of the inertial-to-body attitude at t_k, and $\boldsymbol{v}_{st,k}$ is a small measurement noise rotation vector. Since the noise quaternion is not a proper attitude quaternion, the measurement is normalized to ensure a valid attitude quaternion. The measurement noise is taken to be a zero mean Gaussian random vector with covariance

$$\boldsymbol{P}_{vv,st} = \sigma_{st}^2 \boldsymbol{I}_3\,. \tag{25}$$

3.2 Observability Analysis

Collecting the general dynamics model of Eq. (19) and the general measurement model of Eq. (20) yields a nonlinear, continuous-discrete system of the form

$$\dot{\boldsymbol{x}}(t) = \boldsymbol{f}(\boldsymbol{x}(t), \boldsymbol{u}(t), \boldsymbol{w}(t)) \tag{26a}$$

$$\boldsymbol{z}_k = \boldsymbol{h}(\boldsymbol{x}_k, \boldsymbol{v}_k)\,. \tag{26b}$$

To assess observability of the state of the system, two alterations are made. The first alteration is that the injection of noise is removed from both the dynamical system model and the measurement model. Thus, the dynamics and measurements become deterministic. The second alteration is that continuous-time observations are considered, as opposed to discrete-time measurements, representing a limiting case of the information that is obtainable through observations. The result is that the system under consideration becomes

$$\dot{\boldsymbol{x}}(t) = \boldsymbol{f}(\boldsymbol{x}(t), \boldsymbol{u}(t)) \tag{27a}$$

$$\boldsymbol{y}(t) = \boldsymbol{h}(\boldsymbol{x}(t))\,, \tag{27b}$$

which is an idealization of the true system in which $\boldsymbol{y}(t)$ is used to designate that continuous-time observations are output instead of discrete-time measurements.

3.2.1 Linearized Observability

It is clear from either Eq. (8) or Eq. (9) that the dynamics under consideration are, in general, nonlinear. While Eq. (21) represents a linear mapping of the states into measurements, Eq. (24) is a nonlinaer function of the states. One popular approach in assessing observability of a nonlinear system is to linearize the system about a reference condition. This is accomplished by taking a Taylor series expansion of Eqs. (27) about a nominal state and control history. Doing so yields a linearized system of the form

$$\dot{\boldsymbol{x}}(t) = \boldsymbol{A}(t)\boldsymbol{x}(t) + \boldsymbol{B}(t)\boldsymbol{u}(t) \tag{28a}$$

$$\boldsymbol{y}(t) = \boldsymbol{C}(t)\boldsymbol{x}(t)\,, \tag{28b}$$

where $\boldsymbol{x}(t)$, $\boldsymbol{u}(t)$, and $\boldsymbol{y}(t)$ now represent deviations in the state, control, and output away from the nominal conditions, $\hat{\boldsymbol{x}}(t)$, $\hat{\boldsymbol{u}}(t)$, and $\hat{\boldsymbol{y}}(t)$, respectively, and the mapping matrices are given by

$$\boldsymbol{A}(t) = \left.\frac{\partial \boldsymbol{f}(\boldsymbol{x}(t), \boldsymbol{u}(t))}{\partial \boldsymbol{x}(t)}\right|_{\substack{\boldsymbol{x}(t)=\hat{\boldsymbol{x}}(t) \\ \boldsymbol{u}(t)=\hat{\boldsymbol{u}}(t)}} \tag{29a}$$

$$\boldsymbol{B}(t) = \left.\frac{\partial \boldsymbol{f}(\boldsymbol{x}(t), \boldsymbol{u}(t))}{\partial \boldsymbol{u}(t)}\right|_{\substack{\boldsymbol{x}(t)=\hat{\boldsymbol{x}}(t) \\ \boldsymbol{u}(t)=\hat{\boldsymbol{u}}(t)}} \tag{29b}$$

$$\boldsymbol{C}(t) = \left.\frac{\partial \boldsymbol{h}(\boldsymbol{x}(t)}{\partial \boldsymbol{x}(t)}\right|_{\boldsymbol{x}(t)=\hat{\boldsymbol{x}}(t)}\,. \tag{29c}$$

A system of the form of Eqs. (28) is observable if and only if some time interval exists wherein the system initial conditions can be completely reconstructed from the time history of the outputs [10]. This concept is formalized in the observability Gramian,

$$\boldsymbol{\mathcal{O}}(t) = \int_0^t \boldsymbol{\Phi}^T(\tau)\boldsymbol{C}^T(\tau)\boldsymbol{C}(\tau)\boldsymbol{\Phi}(\tau)\mathrm{d}\tau\,, \tag{30}$$

where $\boldsymbol{\Phi}(t)$ is the state transition matrix which maps the state vector from the initial time to the current time. A system is observable in the time interval $[0 \quad t]$ if and only if the observability Gramian, $\boldsymbol{\mathcal{O}}(t)$, is invertible (or equivalently the determinant of the Gramian is nonzero or it is full rank). Unfortunately, Eq. (30) does not lend itself to convenient computation, since, in general, the state transition matrix must be numerically integrated according to the ordinary differential equation (ODE)

$$\frac{\mathrm{d}}{\mathrm{d}t}\boldsymbol{\Phi}(t) = \boldsymbol{A}(t)\boldsymbol{\Phi}(t)\,. \tag{31}$$

A more convenient approach is to differentiate Eq. (30) with respect to time in order to obtain an ODE for the observability Gramian of the form

$$\frac{\mathrm{d}}{\mathrm{d}t}\boldsymbol{\mathcal{O}}(t) = \boldsymbol{A}^T(t)\boldsymbol{\mathcal{O}}(t) + \boldsymbol{\mathcal{O}}(t)\boldsymbol{A}(t) + \boldsymbol{C}^T(t)\boldsymbol{C}(t)\,. \tag{32}$$

subject to the initial condition that $\boldsymbol{\mathcal{O}}(t_0) = \mathbf{0}_{n_x \times n_x}$, which is an n_x-dimensional square matrix of zeros, where n_x is the dimension of the state, $\boldsymbol{x}(t)$. The ODE given in Eq. (32) can be numerically integrated using any number of widely available routines. At different points in time, the output of the numerical integration procedure can be tested to see if $\boldsymbol{\mathcal{O}}(t)$ is invertible.

3.2.2 Nonlinear Observability

For nonlinear systems, such as the one given by Eqs. (27), assessing global observability is generally infeasible, but local observability for a neighborhood of control signals can be assessed by constructing a generalization to the observability matrix that arises in the case of linear time invariant systems [14, 15, 27]. This nonlinear observability matrix is the gradient of a vector comprising the Lie derivatives of order zero to $(n_x - 1)$ of the observation equations with respect to the dynamics function. This matrix takes the form

$$\boldsymbol{\mathcal{O}} = \begin{bmatrix} \boldsymbol{\mathcal{O}}^1 \\ \boldsymbol{\mathcal{O}}^2 \\ \vdots \\ \boldsymbol{\mathcal{O}}^{n_x} \end{bmatrix} = \frac{\partial}{\partial \boldsymbol{x}} \begin{bmatrix} \boldsymbol{h}(\boldsymbol{x}) \\ \boldsymbol{\mathcal{O}}^1\boldsymbol{f}(\boldsymbol{x},\boldsymbol{u}) \\ \vdots \\ \boldsymbol{\mathcal{O}}^{n_x-1}\boldsymbol{f}(\boldsymbol{x},\boldsymbol{u}) \end{bmatrix} = \frac{\partial}{\partial \boldsymbol{x}} \begin{bmatrix} \boldsymbol{h}(\boldsymbol{x}) \\ L_f^1\{\boldsymbol{h}(\boldsymbol{x})\} \\ \vdots \\ L_f^{n_x-1}\{\boldsymbol{h}(\boldsymbol{x})\} \end{bmatrix}, \tag{33}$$

where n_x is the dimension of the state, $\boldsymbol{x}(t)$, and

$$\boldsymbol{\mathcal{O}}^1 = \frac{\partial \boldsymbol{h}(\boldsymbol{x})}{\partial \boldsymbol{x}} \quad \text{and} \quad \boldsymbol{\mathcal{O}}^{k+1} = \frac{\partial}{\partial \boldsymbol{x}}\{\boldsymbol{\mathcal{O}}^k\boldsymbol{f}(\boldsymbol{x},\boldsymbol{u})\}\,. \tag{34}$$

The k^{th} Lie derivative of the i^{th} component of the measurement vector with respect to the dynamics function is

$$L_f^k\{h_i(\boldsymbol{x})\} = \frac{\partial}{\partial \boldsymbol{x}}\big\{L_f^{k-1}\{h_i(\boldsymbol{x})\}\big\}\boldsymbol{f}(\boldsymbol{x},\boldsymbol{u}) \quad \text{for } k \in \mathbb{N}\,, \tag{35}$$

and by definition $L_f^0\{h_i(\boldsymbol{x})\} = h_i(\boldsymbol{x})$. For notational simplicity the k^{th} Lie derivative applied to the observation vector is

$$L_f^k\{\boldsymbol{h}(\boldsymbol{x})\} = \begin{bmatrix} L_f^k\{h_1(\boldsymbol{x})\} & L_f^k\{h_2(\boldsymbol{x})\} & \cdots & L_f^k\{h_{n_y}(\boldsymbol{x})\} \end{bmatrix}^T, \tag{36}$$

where n_y is the dimension of the observation vector, $\boldsymbol{y}(t)$.

If $\boldsymbol{\mathcal{O}}$ is full rank, the system is locally observable. As in the linear time-invariant case, it is not always necessary to compute all n_x terms in $\boldsymbol{\mathcal{O}}$; if there are multiple observations available, $\boldsymbol{\mathcal{O}}$ is often full rank with fewer terms. While this provides a useful theoretical check for the feasibility of constructing an observer, it can be difficult to evaluate the rank of a matrix of involved functions.

3.2.2.1 Approximation of the Observability Matrix

The Lie derivatives in Eq. (33) tend to become more involved as n_x increases, and for large numbers of states and observations, the analytical computation can become infeasible. An approximation of Eq. (33) is presented in Ref. 28 by truncating the Taylor series of $\boldsymbol{\mathcal{O}}$ to second order. This produces a recursion for computing the higher order Lie derivatives. This approximation only requires the computation of the dynamics Jacobian

$$\boldsymbol{J}_f(\boldsymbol{x}(t), \boldsymbol{u}(t)) = \frac{\partial \boldsymbol{f}(\boldsymbol{x}(t), \boldsymbol{u}(t))}{\partial \boldsymbol{x}(t)}\,, \tag{37}$$

the measurement Jacobian

$$\boldsymbol{J}_h(\boldsymbol{x}(t)) = \frac{\partial \boldsymbol{h}(\boldsymbol{x}(t))}{\partial \boldsymbol{x}(t)}\,, \tag{38}$$

and the Hessian of each component of the measurement vector

$$\boldsymbol{H}_{h_i}(\boldsymbol{x}(t)) = \frac{\partial^2 h_i(\boldsymbol{x}(t))}{\partial \boldsymbol{x}(t) \partial \boldsymbol{x}(t)^T}\,. \tag{39}$$

Omitting functional dependencies for ease of notation, the recursion for the i^{th} component of the observation vector is given by

$$\boldsymbol{\mathcal{O}}_i^{k+1} = \boldsymbol{\mathcal{O}}_i^k \boldsymbol{J}_f + \frac{1}{2} \boldsymbol{f}^T \left[\boldsymbol{\mathcal{H}}_i^k + (\boldsymbol{\mathcal{H}}_i^k)^T \right] \tag{40}$$

$$\boldsymbol{\mathcal{H}}_i^{k+1} = \frac{1}{2} \left[\boldsymbol{\mathcal{H}}_i^k + (\boldsymbol{\mathcal{H}}_i^k)^T \right] \boldsymbol{J}_f\,, \tag{41}$$

where the recursion is initiated via

$$\boldsymbol{\mathcal{O}}_i^1 = \frac{\partial h_i(\boldsymbol{x})}{\partial \boldsymbol{x}} \quad \text{and} \quad \boldsymbol{\mathcal{H}}_i^1 = \frac{\partial^2 h_i(\boldsymbol{x})}{\partial \boldsymbol{x} \partial \boldsymbol{x}^T}\,. \tag{42}$$

3.2.2.2 Numerical Evaluation

To compare the effect of different trajectories (i.e., time histories of the reference conditions) on observability, it is useful to construct a nonlinear observability Gramian. The matrix $\boldsymbol{\mathcal{O}}$, composed of $n_x n_y \times n_x$ time-varying functions, has linearly independent columns over the time interval $[t_0, t]$ if and only if the matrix

$$\boldsymbol{G}(t) = \int_{t_0}^{t} \boldsymbol{\mathcal{O}}^T(\tau) \boldsymbol{\mathcal{O}}(\tau) \mathrm{d}\tau \tag{43}$$

is nonsingular [29].

In order to use this to numerically evaluate the rank of $\boldsymbol{\mathcal{O}}$, it must be assumed that $\boldsymbol{u}(t)$ and $\boldsymbol{x}(t_0)$ have been determined *a priori*. Any appropriate function of this matrix can then be used as a measure for comparing the observability of candidate trajectories. Some common choices are the determinant, the inverse condition number (the ratio of the smallest eigenvalue of $\boldsymbol{G}$ to the largest eigenvalue), and the unobservability index (the reciprocal of the smallest eigenvalue of $\boldsymbol{G}$) [12, 30]. In this work, the trace of the observability Gramian is chosen, because it is simple to compute, nondecreasing, and, as the sum of the eigenvalues, related to the rank condition of the Gramian.

3.3 Estimation of the Inertia Tensor

Consider a nonlinear, continuous-discrete system of the form of Eqs. (19) and (20), which are repeated (except that the input in omitted for ease of notation) here for reference as

$$\dot{\boldsymbol{x}}(t) = \boldsymbol{f}(\boldsymbol{x}(t), \boldsymbol{w}(t)) \tag{44a}$$

$$\boldsymbol{z}_k = \boldsymbol{h}(\boldsymbol{x}_k, \boldsymbol{v}_k)\,, \tag{44b}$$

subject to equality and inequality constraints of the form

$$\boldsymbol{x}_k^T \boldsymbol{A}_{\text{eq}}^{(i)} \boldsymbol{x}_k = b_{\text{eq}}^{(i)} \tag{45a}$$

$$\boldsymbol{A}_{\text{ineq}} \boldsymbol{x}_k \leq \boldsymbol{b}_{\text{ineq}}\,. \tag{45b}$$

In Eq. (44a), $\boldsymbol{w}(t)$ is a zero-mean, white-noise process with constant power spectral density $\boldsymbol{Q}_{ww}$. In Eq. (44b), $\boldsymbol{v}_k$ is a zero-mean, white-noise sequence with constant covariance $\boldsymbol{P}_{vv}$. The nonlinear dynamics function and the nonlinear measurement function are assumed to be differentiable, and the process noise, $\boldsymbol{w}(t)$, and the measurement noise, $\boldsymbol{v}_k$, are taken to be uncorrelated. The state of the system at time t_0 is characterized by its mean, $\boldsymbol{m}_{x,0}$, and covariance $\boldsymbol{P}_{xx,0}$. Equations (45) represent constraints on the states of the system, where Eq. (45a) is a set of $1 \leq i \leq N_{\text{eq}}$ quadratic equality constraints that must be expressed individually and Eq. (45b) is a set of N_{ineq} linear inequality constraints that can be expressed as a single array of constraint equations.

With regard to the problem considered herein, the state of the system is defined in Eq. (17), and the dynamics of the state are given by Eq. (18). From these definitions, it is seen that no representation of the process noise is required; however, for the sake of generality, process noise is retained in the dynamics representation and utilized in further developments. The measurements utilized in this work are defined either as gyro measurements via Eq. (21) or as star tracker measurements via Eq. (24). There are eight constraints to take into account in this work. Two of these constraints are equality constraints that represent the quaternion unit norm constraint of $\|\bar{\boldsymbol{q}}\| = 1$—one for the quaternion representing the attitude of the vehicle (with respect to an inertial coordinate system) and one for the quaternion representing the attitude of the principal axes (with respect to a body-fixed coordinate system). Each of these constraints can be put into the form of Eq. (45a) via proper selection of $\boldsymbol{A}_{\text{eq}}^{(i)}$ and with $b_{\text{eq}}^{(i)} = 1$. The remaining six constraints are linear inequality constraints that act on the principal moments of inertia and which are given in Eqs. (13a) and (14). These constraints can be represented via proper selection of $\boldsymbol{A}_{\text{ineq}}$ and $\boldsymbol{b}_{\text{ineq}}$ in Eq. (45b). It is worth noting that the constraints are only considered at the discrete instances of time that align with newly received measurements. Effectively, this is assuming that the dynamics do not violate the constraints and that the constraints are to be considered alongside the reception of new measurement information.

The objective of an estimator is to sequentially process newly received data (either gyro or star tracker data) and fuse this information with any existing information on the state to produce an improved understanding of the state. Whenever there are no constraints existing between the states of the system or whenever such constraints are ignored, this results in an unconstrained estimator. Otherwise, a constrained estimator is required.

Two classes of estimators are considered in this work: approximate, linear, minimum mean-square error estimators and approximate Bayesian estimators. Approximate, linear, minimum mean-square error estimators are approximate due to the nonlinear nature of the problem, they are linear in that a linear combination of the measurements is employed in the data processing step, and they formulate the update in a way that minimizes the mean-square error of the state after the data has been processed. This formulation gives rise to the class of Kalman filters applied to

nonlinear systems. Approximate Bayesian estimators attempt to estimate the entire probability density function (PDF) of the state, conditioned on the stochastic measurement history. They are approximate because, except in specific cases, an infinite number of parameters is required to completely describe the conditional state PDF. This formulation underpins the class of filters known as particle filters.

To develop a constrained estimator, the unconstrained extended Kalman filter is considered first. To account for the equality constraints imposed on the attitude representations within the state of the system, the multiplicative extended Kalman filter is presented. To account for the inequality constraints that come about due to the presence of constraints on the principal moments of inertia, an approach based on constrained optimization is developed. Following these developments, Gaussian particle flow is considered. As in the Kalman filter approach, the multiplicative framework is utilized to account for the attitude representations in the state. The inequality constraints on the principal moments of inertia are enforced explicitly on each particle to produce a boundary-sticking particle flow update.

3.3.1 Extended Kalman Filter

The extended Kalman filter (EKF) is an ubiquitous approach for estimating the state of nonlinear systems, in which the nonlinear dynamics and nonlinear measurements functions are linearized about the current estimated state via a first-order Taylor series expansion. The EKF is typically represented as a two-stage process, where the first stage propagates a state estimate and uncertainty representation forward in time according to the dynamics of the system, and the second stage updates the state estimate and representation of uncertainty given new measurement data. As the EKF is so widely used, only a brief summary of the method is presented here.

Given the mean and covariance of the state at time t_{k-1}, the propagation stage applies the dynamical system to move these quantities forward to time t_k. The propagation is accomplished by numerically integrating the state estimate and the covariance matrix according to the ODEs

$$\dot{\boldsymbol{m}}_x(t) = \boldsymbol{f}(\boldsymbol{m}_x(t), \boldsymbol{0}_{n_w}) \tag{46a}$$

$$\dot{\boldsymbol{P}}_{xx}(t) = \boldsymbol{F}_x(t)\boldsymbol{P}_{xx}(t) + \boldsymbol{P}_{xx}(t)\boldsymbol{F}_x^T(t) + \boldsymbol{F}_w(t)\boldsymbol{Q}_{ww}\boldsymbol{F}_w^T(t)\,, \tag{46b}$$

where n_w is the dimension of the process noise, $\boldsymbol{F}_x(\cdot)$ is the dynamics Jacobian relative to the state, and $\boldsymbol{F}_w(\cdot)$ is the dynamics Jacobian relative to the process noise, i.e.,

$$\boldsymbol{F}_x(t) = \left.\frac{\partial \boldsymbol{f}(\boldsymbol{x}(t), \boldsymbol{w}(t))}{\partial \boldsymbol{x}(t)}\right|_{\substack{\boldsymbol{x}(t)=\boldsymbol{m}_x(t) \\ \boldsymbol{w}(t)=\boldsymbol{0}_{n_w}}} \tag{47a}$$

$$\boldsymbol{F}_w(t) = \left.\frac{\partial \boldsymbol{f}(\boldsymbol{x}(t), \boldsymbol{w}(t))}{\partial \boldsymbol{w}(t)}\right|_{\substack{\boldsymbol{x}(t)=\boldsymbol{m}_x(t) \\ \boldsymbol{w}(t)=\boldsymbol{0}_{n_w}}} \tag{47b}$$

The ODEs in Eqs. (46) are numerically integrated from an initial time of $t = t_{k-1}$ to a final time of $t = t_k$, subject to the initial conditions

$$\boldsymbol{m}_x(t_{k-1}) = \boldsymbol{m}_{x,k-1}^+ \tag{48a}$$

$$\boldsymbol{P}_{xx}(t_{k-1}) = \boldsymbol{P}_{xx,k-1}^+\,, \tag{48b}$$

which are the *a posteriori* state estimate and covariance at time t_{k-1}. The numerical integration produces, as the final conditions, the *a priori* state estimate and covariance at time t_k, i.e.,

$$\boldsymbol{m}_{x,k}^- = \boldsymbol{m}_x(t_k) \tag{49a}$$

$$\boldsymbol{P}_{xx,k}^- = \boldsymbol{P}_{xx}(t_k)\,. \tag{49b}$$

The update stage of the EKF takes the outputs of the propagation stage, referred to as the *a priori* state estimate and covariance, and fuses this information with the newly received measurement data. The updated, or *a posteriori*, state estimate and covariance are given for any linear gain, $\boldsymbol{K}_k$, by

$$\boldsymbol{m}_{x,k}^{+} = \boldsymbol{m}_{x,k}^{-} + \boldsymbol{K}_k\big(\boldsymbol{z}_k - \boldsymbol{m}_{z,k}^{-}\big) \tag{50a}$$

$$\boldsymbol{P}_{xx,k}^{+} = \big(\boldsymbol{I}_{n_x} - \boldsymbol{K}_k\boldsymbol{H}_{x,k}^{-}\big)\boldsymbol{P}_{xx,k}^{-}\big(\boldsymbol{I}_{n_x} - \boldsymbol{K}_k\boldsymbol{H}_{x,k}^{-}\big)^T + \boldsymbol{K}_k\boldsymbol{H}_{v,k}^{-}\boldsymbol{P}_{vv}(\boldsymbol{H}_{v,k}^{-})^T\boldsymbol{K}_k^T\,, \tag{50b}$$

where $\boldsymbol{m}_{z,k}^{-}$ is the predicted measurement, and $\boldsymbol{H}_{x,k}^{-}$ and $\boldsymbol{H}_{v,k}^{-}$ are the measurement Jacobians relative to the state and the measurement noise, respectively, which are defined as

$$\boldsymbol{H}_{x,k}^{-} = \left.\frac{\partial \boldsymbol{h}(\boldsymbol{x}_k, \boldsymbol{v}_k)}{\partial \boldsymbol{x}_k}\right|_{\substack{\boldsymbol{x}_k = \boldsymbol{m}_{x,k}^{-} \\ \boldsymbol{v}_k = \boldsymbol{0}_{n_v}}} \tag{51a}$$

$$\boldsymbol{H}_{v,k}^{-} = \left.\frac{\partial \boldsymbol{h}(\boldsymbol{x}_k, \boldsymbol{v}_k)}{\partial \boldsymbol{v}_k}\right|_{\substack{\boldsymbol{x}_k = \boldsymbol{m}_{x,k}^{-} \\ \boldsymbol{v}_k = \boldsymbol{0}_{n_v}}}. \tag{51b}$$

Whereas the update generated by the application of Eqs. (50) is valid for any linear gain, it is often desired to intelligently select the gain. To this end, the Kalman gain, given by

$$\boldsymbol{K}_k = \boldsymbol{P}_{xz,k}^{-}(\boldsymbol{P}_{zz,k}^{-})^{-1}\,, \tag{52}$$

is selected to minimize the *a posteriori* mean-square estimation error, where $\boldsymbol{P}_{xz,k}^{-}$ is the cross-covariance between the state and measurement and $\boldsymbol{P}_{zz,k}^{-}$ is the innovation covariance. To complete the update, the predicted measurement, cross-covariance, and innovation covariance are required, which, for the EKF, are computed as

$$\boldsymbol{m}_{z,k}^{-} = \boldsymbol{h}(\boldsymbol{m}_{x,k}^{-}, \boldsymbol{0}_{n_v}) \tag{53a}$$

$$\boldsymbol{P}_{xz,k}^{-} = \boldsymbol{P}_{xx,k}^{-}(\boldsymbol{H}_{x,k}^{-})^T \tag{53b}$$

$$\boldsymbol{P}_{zz,k}^{-} = \boldsymbol{H}_{x,k}^{-}\boldsymbol{P}_{xx,k}^{-}(\boldsymbol{H}_{x,k}^{-})^T + \boldsymbol{H}_{v,k}^{-}\boldsymbol{P}_{vv}(\boldsymbol{H}_{v,k}^{-})^T\,. \tag{53c}$$

The updated mean and covariance become the initial conditions for the next propagation stage of the EKF, and thus the recursive application of the propagation and update stages continues until all data are processed. This procedure is initialized using the prescribed initial conditions on the mean and covariance, given by $\boldsymbol{m}_{x,0}$ and $\boldsymbol{P}_{xx,0}$, respectively.

It should be noted that the EKF is an unconstrained estimator that assumes the states of the system are additive (i.e., adding two states yields another valid state), and a similar assumption is applied to the measurements. The latter of these assumptions is violated whenever measurements cannot be added to one another, such as in the case of unit vector measurements. When this occurs, the innovation, given by $(\boldsymbol{z}_k - \boldsymbol{m}_{z,k}^{-})$, does not represent a valid operation. In these instances, an alteration to the innovation definition, such as a multiplicative innovation [31], is required. The unconstrained nature of the EKF also means that no equality or inequality constraints are enforced through the prescribed procedure for estimating the state of the system.

3.3.2 Multiplicative Extended Kalman Filter

The multiplicative EKF (MEKF) is an alteration to the EKF to handle quaternion states and, therefore, the unit norm constraint that exists for the quaternion. The MEKF uses the quaternion

representation of attitude to globally and nonsingularly represent the attitude, and it uses a three-parameter representation of attitude, such as the rotation vector, to represent deviations away from the global reference. In this way, the quaternion is maintained in the state estimate (the mean), but the minimal representation is maintained in the so-called "error state," which is used to formulate the covariance matrix.

In the application of this paper, there are two attitude quaternions in the state vector. The first attitude quaternion represents the attitude of a body-fixed coordinate system with respect to an inertial coordinate system, and the second attitude quaternion represents the attitude of the same body-fixed coordinate system with respect to a principal axis coordinate system in which the inertia tensor is diagonal. As such, two applications of representing the attitude using a quaternion in the estimate and using the rotation vector in the covariance are required. Recall from Eq. (17) that the state is defined as

$$\boldsymbol{x}^T = [\bar{\boldsymbol{q}}^T \quad \boldsymbol{\omega}^T \quad \boldsymbol{b}_g^T \quad (\boldsymbol{\jmath}_m^p)^T \quad (\bar{\boldsymbol{q}}_p^b)^T] \,, \tag{54}$$

where the time-dependence of the state elements is omitted for brevity. The mean, or estimated state, is given by

$$\boldsymbol{m}_x^T = [\hat{\bar{\boldsymbol{q}}}^T \quad \hat{\boldsymbol{\omega}}^T \quad \hat{\boldsymbol{b}}_g^T \quad (\hat{\boldsymbol{\jmath}}_m^p)^T \quad (\hat{\bar{\boldsymbol{q}}}_p^b)^T] \,, \tag{55}$$

which can be expressed at any instant in time, continuous or discrete, and which can be expressed either prior to or after a measurement update occurs. The usual definition of the state estimation error, given by $\boldsymbol{e}_x = \boldsymbol{x} - \boldsymbol{m}_x$ is only valid for additive, or Euclidean, states. For the two quaternions in the state vector, this definition does not hold. Instead, a multiplicative definition is applied, such that the error state is

$$\boldsymbol{e}_x^T = [\delta\boldsymbol{\phi}^T \quad \delta\boldsymbol{\omega}^T \quad \delta\boldsymbol{b}_g^T \quad (\delta\boldsymbol{\jmath}_m^p)^T \quad (\delta\boldsymbol{\phi}_p^b)^T] \,, \tag{56}$$

where the individual errors are defined as

$$\begin{gathered} \delta\boldsymbol{\phi} = 2\text{vec}\{\bar{\boldsymbol{q}} \otimes \hat{\bar{\boldsymbol{q}}}^{-1}\} \,, \quad \delta\boldsymbol{\omega} = \boldsymbol{\omega} - \hat{\boldsymbol{\omega}} \,, \quad \delta\boldsymbol{b}_g = \boldsymbol{b}_g - \hat{\boldsymbol{b}}_g \,, \\ \delta\boldsymbol{\jmath}_m^p = \boldsymbol{\jmath}_m^p - \hat{\boldsymbol{\jmath}}_m^p \,, \quad \text{and} \quad \delta\boldsymbol{\phi}_p^b = 2\text{vec}\{\bar{\boldsymbol{q}}_p^b \otimes (\hat{\bar{\boldsymbol{q}}}_p^b)^{-1}\} \,. \end{gathered} \tag{57}$$

The vec$\{\cdot\}$ operator appearing in the definitions of the two attitude error states extracts the vector part of the resulting quaternion product. These attitude errors are commonly associated with small-angle errors, which is where the factor of 2 comes from; as such, there is some limitation associated with this representation of the error state.

The propagation stage of the MEKF mirrors that of the EKF. Both the mean and the covariance are (in general) numerically integrated. The quaternion representation(s) of attitude are used for propagating the mean, leveraging attitude kinematics as needed. For the covariance, the dynamics of the error state are considered. This is accomplished by differentiating $\boldsymbol{e}_x$, as defined in Eq. (56), with respect to time and substituting for the full-state dynamics. The resulting system is linearized using a first-order Taylor series expansion, and the result is a linearized system of the form

$$\dot{\boldsymbol{e}}_x(t) = \boldsymbol{F}_x(t)\boldsymbol{e}_x(t) + \boldsymbol{F}_w(t)\boldsymbol{w}(t) \,, \tag{58}$$

which produces the dynamics Jacobians defined in Eqs. (47) and used in Eq. (46b). The size of the system state space for the state defined in Eq. (54) is $n_x = 17$, but, since the system state contains two attitude quaternions, the error space of the system is only size $n_e = 15$. This means that the

state covariance, $\boldsymbol{P}_{xx}$, and the dynamics Jacobian, $\boldsymbol{F}_x$, are both size $n_e \times n_e$. Likewise, the Jacobian $\boldsymbol{F}_w$ is size $n_e \times n_w$.

To process measurements with the MEKF, a similar process is required. A first-order Taylor series is applied to the nonlinear measurement function, making use of the three-parameter representation of attitude to develop a mapping between the measurements and the error state. This same process is also used when attitude measurements are considered, such that multiplicative innovations and small-angle approximations are considered in place of additive models. For the measurements considered in this work, i.e., gyro and star tracker measurements, it can be shown that the mapping from the error space of the system to the measurement space results in the measurement Jacobians

$$\boldsymbol{H}_x = \begin{bmatrix} \boldsymbol{0}_{3\times3} & \boldsymbol{I}_3 & \boldsymbol{I}_3 & \boldsymbol{0}_{3\times6} \\ \boldsymbol{I}_3 & \boldsymbol{0}_{3\times3} & \boldsymbol{0}_{3\times3} & \boldsymbol{0}_{3\times6} \end{bmatrix} \tag{59a}$$

$$\boldsymbol{H}_v = \boldsymbol{I}_6 \,. \tag{59b}$$

In the same way that dimensional alterations are encountered in the propagation stage of the MEKF, the size of the measurement space is $n_z = 7$, but, since one of those measurements is an attitude quaternion, the size of the innovation space is $n_r = 6$. Therefore, the Jacobian $\boldsymbol{H}_x$ is dimension $n_r \times n_e$, and the Jacobian $\boldsymbol{H}_v$ is $n_r \times n_r$.

Given the innovation, $\boldsymbol{e}^-_{z,k} = \left(\boldsymbol{z}_k - \boldsymbol{m}^-_{z,k}\right)$, which is either computed additively as shown or multiplicatively when quaternion measurements are involved, the update to the state estimate is generated as $\Delta\boldsymbol{m}_{x,k} = \boldsymbol{K}_k\boldsymbol{e}^-_{z,k}$. For any additive/Euclidean states, the updated state is computed by adding the corresponding elements of $\Delta\boldsymbol{m}_{x,k}$ to $\boldsymbol{m}^-_{x,k}$ to determine the posterior state estimate. For non-additive/quaternion states, however, the corresponding elements of $\Delta\boldsymbol{m}_{x,k}$ represent small-angle updates to the prior attitude quaternion. As such, these elements of the update are applied using quaternion multiplication, a small-angle assumption, and brute-force normalization of the posterior quaternion estimates to complete the update. Since the covariance is always maintained in the error-space, no additional modifications are required for the covariance update.

3.3.3 Inequality-Constrained Multiplicative Extended Kalman Filter

The MEKF, as presented, handles the two equality constraints represented by Eq. (45a). The six inequality constraints of Eq. (45b), however, must still be addressed. Thus, the inequality-constrained MEKF (ICMEKF) inherits the propagation stage of the MEKF and the multiplicative representation of attitude errors via the error-state formulation.

To proceed, note that the family of Kalman filters are generated via an optimization problem. Given a linear update that takes the form of Eq. (50a), the gain $\boldsymbol{K}_k$ is chosen to minimize the posterior mean-square estimation error, i.e., the cost function is

$$J = \mathbb{E}\{\|\boldsymbol{x}_k - \boldsymbol{m}^+_{x,k}\|^2\} \,, \tag{60}$$

where $\mathbb{E}\{\cdot\}$ is the expectation operator. Minimizing the posterior mean-square estimation error is equivalent to minimizing the trace of the posterior covariance matrix, leading to

$$J = \mathrm{tr}\{\boldsymbol{P}^+_{xx,k}\} \,, \tag{61}$$

where $\mathrm{tr}\{\cdot\}$ represents the matrix trace. It is important to utilize a form of the covariance update in Eq. (61) that is valid for any linear gain. The form used in Eq. (50b) is the Joseph form, which is valid for any linear gain. From Eq. (50b), it is clear that the cost function is quadratic in the elements of the gain.

The optimization formulation that results from choosing $\boldsymbol{K}_k$ to minimize the cost function of Eq. (61) is unconstrained, and selecting $\boldsymbol{K}_k$ according to this optimization problem results in the Kalman gain given in Eq. (52). The elements of $\boldsymbol{K}_k$ are not, however, independent. They must be selected such that the inequality constraints of Eq. (45b), which are constraints on the states of the system, are satisfied. These inequality constraints on the states can be restated as constraints on the elements of the linear gain by considering the state estimate update in conjunction with the inequality constraints. That is, under the assumption that the prior state estimate satisfies the constraints, the gain $\boldsymbol{K}_k$ must be chosen such that the posterior state estimate also satisfies the constraints. Applying the constraints of Eq. (45b) to the update of Eq. (50a), it follows that

$$\boldsymbol{A}_{\text{ineq}}\boldsymbol{K}_k\boldsymbol{e}_{z,k}^{-} \leq \boldsymbol{b}_{\text{ineq}} - \boldsymbol{A}_{\text{ineq}}\boldsymbol{m}_{x,k}^{-} \tag{62}$$

where $\boldsymbol{e}_{z,k}^{-}$ is used to represent the innovation, which can be computed additively or multiplicatively. The structure of Eq. (62) indicates that this remains a set of linear inequality constraints, but now it is formulated as constraints on the elements of $\boldsymbol{K}_k$ instead of constraints on the states.

The optimization formulation of Eq. (61) is quadratic in the elements of $\boldsymbol{K}_k$, and the inequality constraints of Eq. (62) are linear in the elements of $\boldsymbol{K}_k$. This construction is naturally aligned to the quadratic programming problem construct formulated as

$$\text{minimize} \quad \frac{1}{2}\boldsymbol{x}^T\boldsymbol{Q}\boldsymbol{x} + \boldsymbol{g}^T\boldsymbol{x} \tag{63a}$$

$$\text{subject to} \quad \boldsymbol{M}\boldsymbol{x} \leq \boldsymbol{\ell}\,, \tag{63b}$$

where $\boldsymbol{x}$ are the parameters to be selected. All that remains is to convert Eqs. (61) and (62) into the forms of Eqs. (63). To make the necessary conversions, vectorization of the Kalman gain, denoted by $\boldsymbol{k}_k = \text{vec}\{\boldsymbol{K}_k\}$ is used to establish a vector of optimization variables. Note that this is a different use of vec$\{\cdot\}$ from its previous use, but the context should resolve any ambiguity. Additionally, the Kronecker product, which is denoted via $\boldsymbol{A} \otimes_K \boldsymbol{B}$ for some inputs $\boldsymbol{A}$ and $\boldsymbol{B}$, is leveraged. Note that the subscript K distinguishes between the Kronecker product and quaternion multiplication. In particular, the following properties of the Kronecker product are used [32]

$$\text{tr}\{\boldsymbol{A}_1\boldsymbol{A}_2\boldsymbol{A}_3\} = \text{vec}\{\boldsymbol{A}_3^T\}^T\big(\boldsymbol{A}_2^T \otimes_K \boldsymbol{I}\big)\text{vec}\{\boldsymbol{A}_1\} \tag{64a}$$

$$\text{vec}\{\boldsymbol{A}_1\boldsymbol{A}_2\boldsymbol{A}_3\} = \big(\boldsymbol{A}_3^T \otimes_K \boldsymbol{A}_1\big)\text{vec}\{\boldsymbol{A}_2\}\,. \tag{64b}$$

First, consider the optimization problem of Eq. (61). Applying the covariance update of Eq. (50b), distributing the trace operation to each term, and reducing, it follows that

$$\text{tr}\{\boldsymbol{P}_{xx,k}^{+}\} = \text{tr}\{\boldsymbol{P}_{xx,k}^{-}\} - 2\text{tr}\{\boldsymbol{K}_k(\boldsymbol{P}_{xz,k}^{-})^T\} + \text{tr}\{\boldsymbol{K}_k\boldsymbol{P}_{zz,k}^{-}\boldsymbol{K}_k^T\}\,. \tag{65}$$

Now, the property of Eq. (64a) is applied to each of the last two terms of Eq. (65). For the next-to-last term, $\boldsymbol{A}_1 = \boldsymbol{K}_k$, $\boldsymbol{A}_2 = \boldsymbol{I}$, and $\boldsymbol{A}_3 = (\boldsymbol{P}_{xz,k}^{-})^T$. For the last term, $\boldsymbol{A}_1 = \boldsymbol{K}_k$, $\boldsymbol{A}_2 = \boldsymbol{P}_{zz,k}^{-}$, and $\boldsymbol{A}_3 = \boldsymbol{K}_k^T$. The result is that the cost function can be expressed as

$$\text{tr}\{\boldsymbol{P}_{xx,k}^{+}\} = \text{tr}\{\boldsymbol{P}_{xx,k}^{-}\} - 2\text{vec}\{\boldsymbol{P}_{xz,k}^{-}\}^T\boldsymbol{k}_k + \boldsymbol{k}_k^T\big(\boldsymbol{P}_{zz,k}^{-} \otimes_K \boldsymbol{I}_{n_e}\big)\boldsymbol{k}_k\,, \tag{66}$$

which is quadratic in the vectorized elements of the linear gain, as expected.

Next, consider the linear inequality constraints of Eq. (62). Noting that this relationship is already a vector expression, vectorization of it does not alter it. Therefore, the property of Eq. (64b) is applied with $\boldsymbol{A}_1 = \boldsymbol{A}_{\text{ineq}}$, $\boldsymbol{A}_2 = \boldsymbol{K}_k$, and $\boldsymbol{A}_3 = \boldsymbol{e}_{z,k}^{-}$ to yield

$$\big((\boldsymbol{e}_{z,k}^{-})^T \otimes_K \boldsymbol{A}_{\text{ineq}}\big)\boldsymbol{k}_k \leq \boldsymbol{b}_{\text{ineq}} - \boldsymbol{A}_{\text{ineq}}\boldsymbol{m}_{x,k}^{-}\,, \tag{67}$$

which is linear in the vectorized elements of the linear gain, as expected.

Finally, the results of Eqs. (66) and (67) are compared to the formulation of Eqs. (63) to establish the forms for the inputs to the optimization problem. This produces the equivalences of

$$\boldsymbol{Q} = 2\big(\boldsymbol{P}^{-}_{zz,k} \otimes_K \boldsymbol{I}_{n_e}\big) \tag{68a}$$

$$\boldsymbol{g} = -2\text{vec}\{\boldsymbol{P}^{-}_{xz,k}\}^T \tag{68b}$$

$$\boldsymbol{M} = \big((\boldsymbol{e}^{-}_{z,k})^T \otimes_K \boldsymbol{A}_{\text{ineq}}\big) \tag{68c}$$

$$\boldsymbol{\ell} = \boldsymbol{b}_{\text{ineq}} - \boldsymbol{A}_{\text{ineq}}\boldsymbol{m}^{-}_{x,k}\,. \tag{68d}$$

where, from the structure of the inequality constraints of Eqs. (13a) and (14), $\boldsymbol{b}_{\text{ineq}} = \boldsymbol{0}_6$ and

$$\boldsymbol{A}_{\text{ineq}} = \left[\begin{array}{c|ccc|c} & 1 & -1 & -1 & \\ & -1 & 1 & -1 & \\ \boldsymbol{0}_{6\times 9} & -1 & -1 & 1 & \boldsymbol{0}_{6\times 3} \\ & -1 & 0 & 0 & \\ & 0 & -1 & 0 & \\ & 0 & 0 & -1 & \end{array}\right], \tag{69}$$

where the first three rows describe the triangle inequality constraints of Eq. (13a) and the last three rows describe the positive definite constraints of Eq. (14). Note that $\boldsymbol{A}_{\text{ineq}}$ is defined relative to the error space, as this is where the update of the ICMEKF is performed. As such, the product $\boldsymbol{A}_{\text{ineq}}\boldsymbol{m}^{-}_{x,k}$ needs to be adjusted. The adjustment is straightforwardly performed by replacing the quaternion states with three-dimensional arrays of zeros before the product is carried out. This results in a valid representation for $\boldsymbol{\ell}$ since none of the linear inequality constraints involves any of the elements of the attitude quaternions.

The update stage of the ICMEKF is performed by solving the optimization problem of Eqs. (63) to find the elements $\boldsymbol{k}_k$. This optimization problem is solved numerically using available library routines, such as `quadprog` in MATLAB. The optimal gain elements are then converted into the linear gain $\boldsymbol{K}_k$, and the update relationships of Eqs. (50) are applied. The result is a posterior estimate that satisfies the state constraints and an associated covariance matrix. It should be noted that numerical issues can influence the solution, such that satisfaction of the constraints in all cases is difficult to guarantee.

3.3.4 Gaussian Particle Flow Filter

Particle filters are approximate Bayesian filters that work by approximating the state PDF as a sum of weighted samples (or particles). These particles can be propagated through the state dynamics to the measurement epoch and updated with the new information. Typically, the update is performed by computing the weight of each particle from the measurement likelihood. Often, the updated weights of many of these particles approach zero; this means that the state PDF is functionally represented by only a fraction of the particles, which can lead to an inaccurate approximation. This problem is referred to as weight degeneracy. One way of avoiding weight degeneracy is to update the PDF by moving the prior set of particles through the state space, rather than updating the weights. This approach is known as particle flow.

3.3.4.1 Exact Gaussian Particle Flow

It is well established that Bayes' rule is the solution to the optimization problem

$$\pi(\boldsymbol{x}) = \underset{q(\boldsymbol{x})}{\arg\min} \left\{ \int q(\boldsymbol{x}) \log \frac{q(\boldsymbol{x})}{p(\boldsymbol{x})} \mathrm{d}\boldsymbol{x} - \int q(\boldsymbol{x}) \log \ell(\boldsymbol{z}|\boldsymbol{x}) \mathrm{d}\boldsymbol{x} \right\}, \tag{70}$$

where $p(\boldsymbol{x})$ is the prior state PDF, and $\ell(\boldsymbol{z}|\boldsymbol{x})$ is the likelihood of the measurement given the state [33]. Note that all time-dependencies are omitted for ease of notation. Equation (70) can be modified as

$$\pi(\boldsymbol{x}) = \underset{q(\boldsymbol{x})}{\arg\min} \left\{ \int q(\boldsymbol{x}) \log \frac{q(\boldsymbol{x})}{p(\boldsymbol{x})} \mathrm{d}\boldsymbol{x} - \tau \int q(\boldsymbol{x}) \log \ell(\boldsymbol{z}|\boldsymbol{x}) \mathrm{d}\boldsymbol{x} \right\}, \tag{71}$$

by adding the homotopy parameter $\tau \in [0, 1]$. When $\tau = 0$, this results in the prior distribution, and, when $\tau = 1$, Eq. (71) returns to the original optimization problem of Eq. (70). The inclusion of this term results in a homotopic Bayes' rule

$$\pi(\boldsymbol{x}) = \frac{\ell^{\tau}(\boldsymbol{z}|\boldsymbol{x}) p(\boldsymbol{x})}{\int \ell^{\tau}(\boldsymbol{z}|\boldsymbol{x}) p(\boldsymbol{x}) \mathrm{d}\boldsymbol{x}} \,. \tag{72}$$

The PDF of the multivariate Gaussian distribution is

$$p_g(\boldsymbol{y}; \boldsymbol{a}, \boldsymbol{B}) = |2\pi \boldsymbol{B}|^{-\frac{1}{2}} \exp\left\{ -\frac{1}{2} (\boldsymbol{y} - \boldsymbol{a})^T \boldsymbol{B}^{-1} (\boldsymbol{y} - \boldsymbol{a}) \right\}, \tag{73}$$

where $\boldsymbol{a}$ is the mean and $\boldsymbol{B}$ is the covariance. If the prior distribution is Gaussian with mean $\boldsymbol{m}$ and covariance $\boldsymbol{P}$,

$$p(\boldsymbol{x}) = p_g(\boldsymbol{x}; \boldsymbol{m}, \boldsymbol{P}), \tag{74}$$

and the measurement likelihood is

$$\ell(\boldsymbol{z}|\boldsymbol{x}) = p_g(\boldsymbol{z}; \boldsymbol{h}(\boldsymbol{x}), \boldsymbol{R}) \,, \tag{75}$$

which is an additive noise model for the measurements, it can be shown that the homotopy for the resulting state PDF is

$$\pi(\boldsymbol{x}, \tau) = p_g(\boldsymbol{x}; \boldsymbol{\mu}(\tau), \boldsymbol{\Pi}(\tau)) \tag{76}$$

where the mean and covariance homotopies are given by [34, 35]

$$\boldsymbol{\mu}(\tau) = \boldsymbol{m} + \boldsymbol{K} \boldsymbol{e}_z \tag{77a}$$

$$\boldsymbol{\Pi}(\tau) = \boldsymbol{P} - \boldsymbol{K} \boldsymbol{H} \boldsymbol{P} \,. \tag{77b}$$

Similar to the MEKF discussion of Section 3.3.3, $\boldsymbol{e}_z$ is the measurement innovation, $\boldsymbol{H}$ is the mapping matrix from the state error space to the innovation space, and $\boldsymbol{K}$ is a gain given by [36]

$$\boldsymbol{K} = \tau \boldsymbol{P} \boldsymbol{H}^T (\tau \boldsymbol{H} \boldsymbol{P} \boldsymbol{H}^T + \boldsymbol{R})^{-1} \,. \tag{78}$$

The particle motion with respect to the pseudo-time, τ, is underdetermined, so a form of the motion must be assumed. If it is assumed that particle motion has two components—the mean motion of

the PDF and some particle contraction—the differential equation that governs the motion of the ℓ^{th} particle takes the form

$$\frac{\mathrm{d}\boldsymbol{x}_\ell}{\mathrm{d}\tau} = \boldsymbol{A}(\boldsymbol{x}_\ell - \boldsymbol{\mu}) + \frac{\mathrm{d}\boldsymbol{\mu}}{\mathrm{d}\tau}\,, \tag{79}$$

where $\boldsymbol{A}$ can be found to be

$$\boldsymbol{A} = -\frac{1}{2}\boldsymbol{P}\boldsymbol{H}^T(\tau\boldsymbol{H}\boldsymbol{P}\boldsymbol{H}^T + \boldsymbol{R})^{-1}\boldsymbol{H}\,. \tag{80}$$

and $\mathrm{d}\boldsymbol{\mu}/\mathrm{d}\tau$ is found by differentiating the mean homotopy relationship of Eq. (77a) with respect to the homotopy parameter, τ.

3.3.4.2 Multiplicative Particle Flow

As with the EKF, including quaternion states in particle flow requires some special considerations. Essentially, a new set of particles is constructed wherein the Euclidean states remain exactly the same, and the attitude states are the three-parameter deviation, $\delta\boldsymbol{a}_\ell$, from the prior mean attitude, $\hat{\bar{\boldsymbol{q}}}$, which can be computed as

$$\delta\bar{\boldsymbol{q}}_\ell^- = \bar{\boldsymbol{q}}_\ell^- \otimes (\hat{\bar{\boldsymbol{q}}}^-)^{-1} = \begin{bmatrix} \frac{1}{2}\delta\boldsymbol{a}_\ell^- \\ 1 \end{bmatrix}\,, \tag{81}$$

where $\bar{\boldsymbol{q}}_\ell^-$ is the prior attitude quaternion of the ℓ^{th} particle. The components of $\boldsymbol{\mu}$ corresponding to attitude states are initialized at $\boldsymbol{0}_3$, since they represent the deviation of the prior attitude mean from itself. To compute the mean of attitude quaternions the matrix

$$\boldsymbol{Q} = \sum_\ell \bar{\boldsymbol{q}}_\ell \bar{\boldsymbol{q}}_\ell^T \tag{82}$$

is constructed. Then, the mean quaternion, $\hat{\bar{\boldsymbol{q}}}$, is the unit eigenvector corresponding to the largest eigenvalue of $\boldsymbol{Q}$ [37]. The posterior attitude quaternions are found by composing the estimated deviations with the prior quaternion,

$$\bar{\boldsymbol{q}}_\ell^+ \propto \begin{bmatrix} \frac{1}{2}\delta\boldsymbol{a}_\ell^+ \\ 1 \end{bmatrix} \otimes \hat{\bar{\boldsymbol{q}}}^-\,, \tag{83}$$

where they must be normalized, since the deviation quaternion does not have a norm of one.

3.3.4.3 Computing Central Moments from Particles

The prior mean and covariance of the particles are required to initiate the particle flow update. For the Euclidean states, the mean is simply the sample mean

$$\boldsymbol{m}_e = \frac{1}{n_p}\sum_{\ell=1}^{n_p} \boldsymbol{x}_{\ell,e}\,, \tag{84}$$

where n_p is the number of particles, and the mean quaternions are computed using Eq. (82) as previously discussed. To compute the covariance, the first step is to evaluate the deviation of each particle from the mean. For the Euclidean states, this is simple subtraction

$$\boldsymbol{e}_{\ell,e} = \boldsymbol{x}_{\ell,e} - \boldsymbol{m}_e\,; \tag{85}$$

for the quaternion states, the process is analogous to computing star tracker innovations, i.e.,

$$\boldsymbol{e}_{\ell,q} = 2\text{vec}\{\bar{\boldsymbol{q}}_\ell \otimes \hat{\bar{\boldsymbol{q}}}^{-1}\}\,. \tag{86}$$

The covariance can then be calculated as the sample covariance of the particle deviations,

$$\boldsymbol{P} = \frac{1}{n_p - 1}\sum_{\ell=1}^{n_p} \boldsymbol{e}_\ell \boldsymbol{e}_\ell^T\,. \tag{87}$$

To enforce inequality constraints, it is straightforward to check which particles satisfy Eq. (13) and Eq. (14) and exclude all others from the computation of the mean and covariance. For linear inequality constraints, if the mean, computed in this manner, is used as the state estimate, it guarantees that the estimate is physically possible and that the covariance is properly represented. It should be noted that, for a general set of nonlinear inequality constraints, this is not necessarily the case.

3.3.4.4 Boundary-Sticking Gaussian Particle Flow Filter

The particle filter implementation described above allows for particles to be updated into a part of the state space that is in violation of state constraints. Since it is possible that all or almost all of the particles will violate the constraints and since such particles are excluded from the computation of the mean and covariance, this allows for complete filter failure to occur. This fragility is undesirable for recursive estimation approaches, especially for onboard implementations. One way to directly mitigate this problem is to only update the particles until they reach the constraint boundary. This is a less theoretically rigorous approach than allowing the particles to exit the constrained state space, because it can skew the conditional PDF toward the constraint boundaries, but it is far more robust. This approach ensures that no particles can violate the constraints, so all of the particles are used in the computation of the mean and covariance.

4.0 RESULTS AND DISCUSSION

4.1 Linearized Inertia Tensor Observability

This section presents numerical simulation results and analysis of the observability of the inertia tensor using the linearized observability analysis presented in Section 3.2.1. Three scenarios are considered, where each scenario is defined by a reference trajectory that is generated from a different control input. Performance is assessed by examining the rank, determinant, and smallest singular value of the observability Gramian for each scenario. Any value smaller than 10^{-10} is considered numerically zero, in the following analysis. The initial conditions for each reference trajectory are taken to be

$$\hat{\bar{\boldsymbol{q}}} = \begin{bmatrix}0.5\\0.5\\0.5\\0.5\end{bmatrix},\ \hat{\boldsymbol{\omega}} = \boldsymbol{0}_3 \text{ rad/s}\,,\ \hat{\boldsymbol{b}}_g = \boldsymbol{0}_3 \text{ rad/s}\,,\ \text{and } \hat{\boldsymbol{J}} = \begin{bmatrix}308.5 & 0.1 & 0.0\\ 0.1 & 402.1 & 4.5\\ 0.0 & 4.5 & 508.8\end{bmatrix} \text{ kg}\cdot\text{m}^2\,, \tag{88}$$

where the values of the inertia tensor are based on the Messenger spacecraft [1].

4.1.1 Linearized System

As discussed in Section 3.2.1, the attitude dynamics of a spacecraft do not constitute a linear system, and some measurements (such as star tracker measurements in this work) are also nonlinear with respect to the state. In both cases, however, the nonlinear models can be linearized and an approximate linear system can be used to facilitate observability analysis. As a reminder, it is also assumed that measurements are continuously available and that there are no stochastic processes acting within the dynamical/measurement system.

In the linearized system, the matrices $\boldsymbol{A}(t)$ and $\boldsymbol{C}(t)$ are the dynamics Jacobian and the measurement Jacobian, respectively, linearized about the reference trajectory $\hat{\boldsymbol{x}}(t)$. For the case of spacecraft attitude dynamics given in Eq. (18) for the state defined by Eq. (17), the dynamics Jacobian is given by

$$\boldsymbol{A}(t) = \begin{bmatrix} -[\hat{\boldsymbol{\omega}}\times] & \boldsymbol{I}_3 & \boldsymbol{0}_{3\times3} & \boldsymbol{0}_{3\times3} & \boldsymbol{0}_{3\times3} \\ \boldsymbol{0}_{3\times3} & \boldsymbol{A}_{2,2} & \boldsymbol{0}_{3\times3} & \boldsymbol{A}_{2,4} & \boldsymbol{A}_{2,5} \\ \boldsymbol{0}_{3\times3} & \boldsymbol{0}_{3\times3} & \boldsymbol{0}_{3\times3} & \boldsymbol{0}_{3\times3} & \boldsymbol{0}_{3\times3} \\ \boldsymbol{0}_{3\times3} & \boldsymbol{0}_{3\times3} & \boldsymbol{0}_{3\times3} & \boldsymbol{0}_{3\times3} & \boldsymbol{0}_{3\times3} \\ \boldsymbol{0}_{3\times3} & \boldsymbol{0}_{3\times3} & \boldsymbol{0}_{3\times3} & \boldsymbol{0}_{3\times3} & \boldsymbol{0}_{3\times3} \end{bmatrix}, \tag{89}$$

where the nontrivial elements of $\boldsymbol{A}(t)$ are given by

$$\boldsymbol{A}_{2,2} = \left[\hat{\boldsymbol{J}} + \sum_{\ell=1}^{n_w} J_\ell^{\parallel}\, \boldsymbol{n}_\ell^{\parallel}\, (\boldsymbol{n}_\ell^{\parallel})^T\right]^{-1} \left\{ [(\hat{\boldsymbol{J}}\hat{\boldsymbol{\omega}} + \hat{\boldsymbol{h}}_w)\times] - [\hat{\boldsymbol{\omega}}\times]\left[\hat{\boldsymbol{J}} + \sum_{\ell=1}^{n_w} J_\ell^{\parallel}\, \boldsymbol{n}_\ell^{\parallel}\, (\boldsymbol{n}_\ell^{\parallel})^T\right]\right\} \tag{90a}$$

$$\boldsymbol{A}_{2,4} = \left[\hat{\boldsymbol{J}} + \sum_{\ell=1}^{n_w} J_\ell^{\parallel}\, \boldsymbol{n}_\ell^{\parallel}\, (\boldsymbol{n}_\ell^{\parallel})^T\right]^{-1} \left\{ \hat{\boldsymbol{J}}[\dot{\hat{\boldsymbol{\omega}}}\times] - [\hat{\boldsymbol{J}}\dot{\hat{\boldsymbol{\omega}}}\times] + [\hat{\boldsymbol{\omega}}\times]\hat{\boldsymbol{J}}[\hat{\boldsymbol{\omega}}\times] - [\hat{\boldsymbol{\omega}}\times][\hat{\boldsymbol{J}}\hat{\boldsymbol{\omega}}\times]\right\} \tag{90b}$$

$$\boldsymbol{A}_{2,5} = -\left[\hat{\boldsymbol{J}} + \sum_{\ell=1}^{n_w} J_\ell^{\parallel}\, \boldsymbol{n}_\ell^{\parallel}\, (\boldsymbol{n}_\ell^{\parallel})^T\right]^{-1} \left\{ \boldsymbol{T}(\hat{\bar{\boldsymbol{q}}}_p^b)[\boldsymbol{T}(\hat{\bar{\boldsymbol{q}}}_p^b)\dot{\hat{\boldsymbol{\omega}}}\backslash] + [\hat{\boldsymbol{\omega}}\times]\boldsymbol{T}(\hat{\bar{\boldsymbol{q}}}_p^b)[\boldsymbol{T}^T(\hat{\bar{\boldsymbol{q}}}_p^b)\hat{\boldsymbol{\omega}}\backslash]\right\}, \tag{90c}$$

and the measurement Jacobian is

$$\boldsymbol{C} = \begin{bmatrix} \boldsymbol{I}_3 & \boldsymbol{0}_{3\times3} & \boldsymbol{0}_{3\times3} & \boldsymbol{0}_{3\times3} & \boldsymbol{0}_{3\times3} \\ \boldsymbol{0}_{3\times3} & \boldsymbol{I}_3 & \boldsymbol{I}_3 & \boldsymbol{0}_{3\times3} & \boldsymbol{0}_{3\times3} \end{bmatrix}. \tag{91}$$

Within the dynamics and measurement Jacobians, any variable with a hat accent ($\hat{\cdot}$) is evaluated along the reference trajectory. Since $\boldsymbol{A}(t)$ explicitly depends on the reference trajectory, the observability Gramian is coupled with the dynamics of the reference trajectory,

$$\dot{\hat{\bar{\boldsymbol{q}}}}(t) = \frac{1}{2}\hat{\boldsymbol{\omega}} \otimes \hat{\bar{\boldsymbol{q}}} \tag{92a}$$

$$\dot{\hat{\boldsymbol{\omega}}}(t) = \left[\hat{\boldsymbol{J}} + \sum_{\ell=1}^{n_w} J_\ell^{\parallel}\, \boldsymbol{n}_\ell^{\parallel}\, (\boldsymbol{n}_\ell^{\parallel})^T\right]^{-1} \left[-\sum_{\ell=1}^{n_w} J_\ell^{\parallel}\, \dot{\omega}_\ell\, \boldsymbol{n}_\ell^{\parallel} - \hat{\boldsymbol{\omega}} \times (\hat{\boldsymbol{J}}\hat{\boldsymbol{\omega}} + \hat{\boldsymbol{h}}_w)\right], \tag{92b}$$

$$\dot{\hat{\boldsymbol{b}}}_g = \boldsymbol{0}_3 \tag{92c}$$

$$\dot{\hat{\boldsymbol{j}}}_m^p = \boldsymbol{0}_3 \tag{92d}$$

$$\dot{\hat{\bar{\boldsymbol{q}}}}_p^b = \boldsymbol{0}_4 \tag{92e}$$

and these differential equations must be solved simultaneously.

4.1.2 Scenario #1: Square Wave

The first control input investigated is a square wave, as shown in Figure (1), where each reaction wheel has the same commanded acceleration profile. Figure (2) shows the determinant of the observability Gramian and its smallest singular value. Clearly, neither approaches a value that can be considered nonzero. The rank of the matrix initially increases to 12—full rank is 15—then stays constant for the duration of the simulation, so its plot is omitted. In spite of the significant stimulation to the system, it remains unobservable with these control signals. From this, it can be concluded that there must be variation in the commanded acceleration of each wheel. That is to say that the control inputs must be varied enough that all states can be disambiguated.

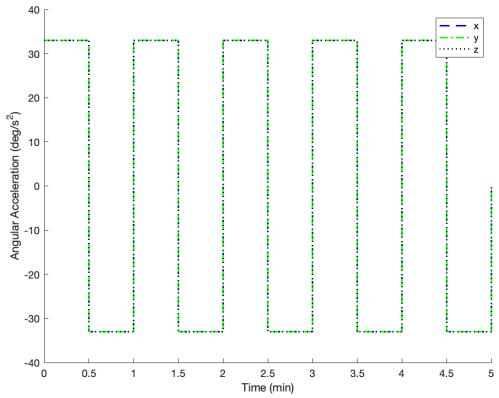

Figure 1. Square wave control input for Scenario #1

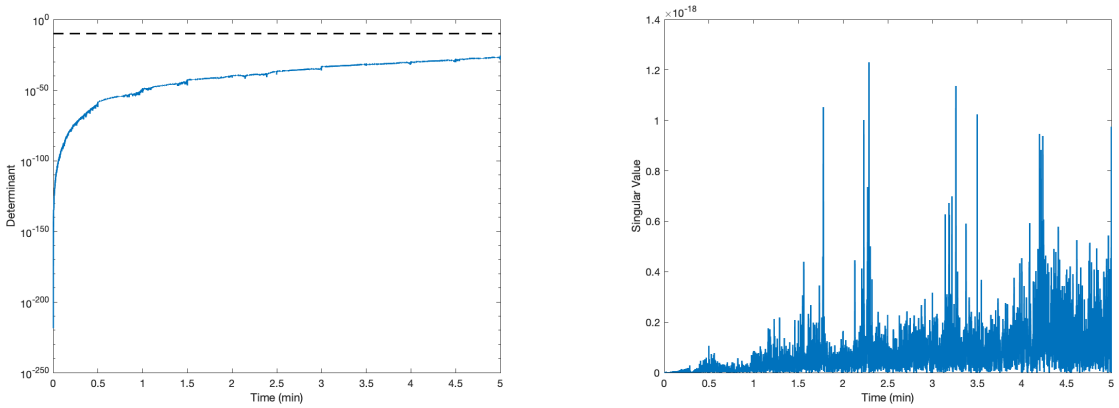

Figure 2. Determinant (left) and smallest singular value (right) of the observability Gramian for Scenario #1

4.1.3 Scenario #2: Individual Wheel Acceleration

In the second scenario, each reaction wheel is accelerated on its own before all three wheels are accelerated together; these angular accelerations are shown in Figure (3). Figure (4) shows the time evolution of the determinant of the observability Gramian. The determinant increases significantly at 1 minute and 2 minutes, and these times correspond directly to the instances that the wheels in

the y and z directions begin to actuate. Furthermore, after 2 minutes, the determinant becomes nonzero, which is mathematically equivalent to the Gramian being invertible. These results, in conjunction with those of the previous case (with uniform signals to each wheel), provide good evidence of the importance of geometrically distinct control signals. It is interesting to note that there is a lag between the time that the determinant becomes nonzero (around 2 minutes) and when the observability Gramian becomes full rank (around 2.3 minutes). The smallest singular value also becomes nonzero around the same time that the Gramian reaches full rank. Probably, this discrepancy is the result of numerical error since the condition number of the observability Gramian is quite high (around 10^{13}).

4.1.4 Scenario #3: Low Amplitude Excitation

It is also worth investigating what role the input amplitude plays in observability. As such, the third scenario is identical to the case presented in Section 4.1.3, but the acceleration amplitude is set to ten percent of the maximum value (where the maximum angular acceleration is 0.576 rad/s^2). Figure (5) shows the reaction wheel accelerations, and Figure (6) illustrates the determinant, smallest singular value, and rank of the observability Gramian. While the determinant and the smallest singular value both increase to nonzero values, the rank of the Gramian never exceeds 14. Furthermore, the rank of the Gramian decreases at several instances, which is not theoretically possible. This odd behavior is the result of a poorly conditioned observability Gramian (condition number on the order of 10^{15}). Clearly, since the only difference between this scenario and the one presented in Section 4.1.3 is the maximum control input, the magnitude of the control input is an important factor.

4.1.5 Summary of Analysis

Sections 4.1.2–4.1.4 investigate the effects of control signals on the observability of spacecraft attitude dynamics with uncertain inertia. Actuation is provided by a set of reaction wheels, and measurements are available from a star tracker and gyro. Linearization is leveraged along with the assumption of continuous, noiseless measurements in order to perform observability analysis. Three control signals are tested: Section 4.1.2 considers a simple square wave with angular acceleration amplitude equal to the maximum possible from the chosen reaction wheels; Section 4.1.3 investigates control signals comprised of one period of the same square wave on each wheel consecutively followed by all wheels actuated together; the control signal of Section 4.1.4 is the same as the second scenario, but with ten percent of the angular acceleration amplitude. Results are assessed by numerically integrating the observability Gramian and analyzing its rank, determinant, and smallest singular value as functions of time.

The results indicate that system observability is sensitive to choice of actuation signal. In particular, numerical errors arise if the amplitude of the signal is not sufficiently large. Furthermore, geometric diversity in the control signal is necessary to effect system observability, as demonstrated by the first simulation. Based on these results, the control signal employed in Scenario #2 is sufficient for system observability. Observability (in the loosest sense) might improve with even larger reaction wheel accelerations, but operational considerations constrain the upper limit.

4.2 Nonlinear Inertia Tensor Observability

This section investigates the determination of control inputs that maximize the observability, leveraging Lie-derivative-based observability analysis. The analysis is carried out using inertia

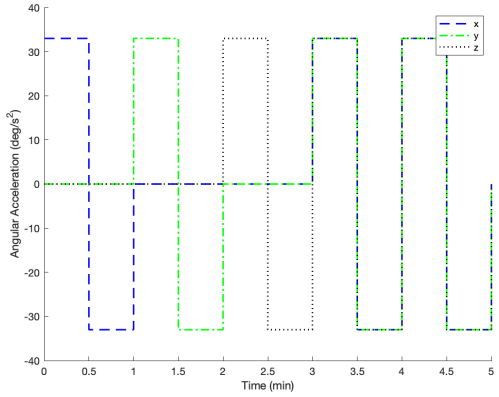

Figure 3. Individual wheel acceleration control input for Scenario #2

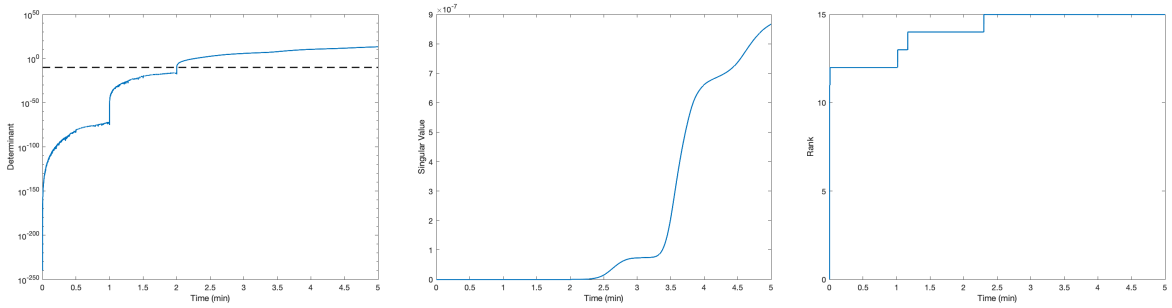

Figure 4. Determinant (left), smallest singular value (middle), and rank (right) of the observability Gramian for Scenario #2

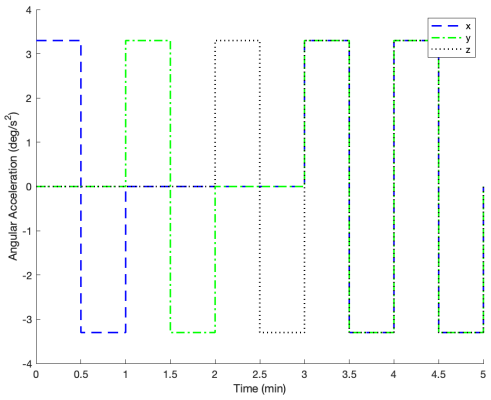

Figure 5. Low amplitude excitation control input for Scenario #3

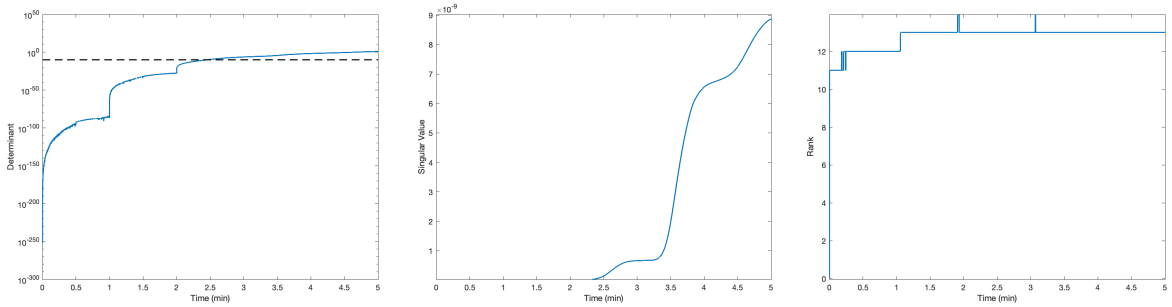

Figure 6. Determinant (left), smallest singular value (middle), and rank (right) of the observability Gramian for Scenario #3

tensor values based on the Messenger Spacecraft [1], such that the body-frame inertia tensor is

$$\boldsymbol{J} = \begin{bmatrix} 308.5 & -0.1 & 0.0 \\ -0.1 & 402.1 & 4.5 \\ 0.0 & 4.5 & 508.8 \end{bmatrix} \text{ kg} \cdot \text{m}^2 \,. \tag{93}$$

Furthermore, the spacecraft is assumed to have zero angular velocity initially, and the maximum torque and angular velocity are conservatively chosen as

$$\tau_{\max} = 1 \text{ Nm} \quad \text{and} \quad \omega_{\max} = 3 \text{ deg/s} \,. \tag{94}$$

The final time is taken to be 5 minutes, and each time step is 5 seconds. Three control sequences are computed: the first is determined by considering a time horizon of one step, the second sequence considers a time horizon of two steps, and the third sequence three steps. These are henceforth referred to as Sequence One, Sequence Two, and Sequence Three, respectively, for ease of reference. For each set of control inputs, the torque and angular velocity are plotted, followed by a comparison of the cost function for each sequence plotted against time.

4.2.1 Optimization

The control input being designed is chosen in order to maximizes the observability, which is measured via $\text{tr}\{\boldsymbol{G}(t_f)\}$, where $\boldsymbol{G}(t)$ is defined in Eq. (43); see Section 3.2.2 for more details. This leads to a minimization problem described by the cost function

$$J = -\text{tr}\{\boldsymbol{G}(t_f)\} \,, \tag{95}$$

for some finite horizon time, t_f, subject to the inequality constraints

$$\|\boldsymbol{\omega}(t)\| \leq \omega_{\max} \quad \forall\, t \in [0, t_f] \tag{96a}$$

$$\|\boldsymbol{\tau}(t)\| \leq \tau_{\max} \quad \forall\, t \in [0, t_f] \,, \tag{96b}$$

and the dynamics in Eq. (16). The control signal is approximated by a sequence of zero-order holds, and the values of each step are computed using an interior point optimization routine, namely `fmincon` in MATLAB. This leads to the cost function

$$J = -\sum_{n=1}^{N} \text{tr}\{\boldsymbol{G}(t_{n-1}, t_n)\} \,. \tag{97}$$

For large numbers of control steps, it is infeasible to compute the entire sequence, so a moving time horizon approach is employed,

$$\min_{\boldsymbol{U}_n} -\text{tr}\{\boldsymbol{G}(t_{n-1}, t_{n+m})\}\,, \tag{98}$$

subject to

$$\|\boldsymbol{\omega}_{b/i}(t_n)\| \leq \omega_{\max} \quad \forall\, n = 1,\ 2, \ldots,\ N \tag{99a}$$

$$\|\boldsymbol{\tau}(t_n)\| \leq \tau_{\max} \quad \forall\, n = 1,\ 2, \ldots,\ N\,, \tag{99b}$$

where $m+1$ is the number of time steps considered, and

$$\boldsymbol{U}_n = [\boldsymbol{u}_n \quad \boldsymbol{u}_{n+1} \quad \cdots \quad \boldsymbol{u}_{n+m}]\,, \tag{100}$$

is a concatenated matrix of control vectors.

In order to forestall numerical complications, the discontinuous control signal is approximated by a piecewise continuous function composed of switching functions of the form

$$f(x) = \frac{y^- - y^+}{2} \tanh\left(\alpha(x - x_d) + 1\right) + y^-\,, \tag{101}$$

where y^- and y^+ are values of the function before and after the discontinuity, respectively, x_d is the location of the discontinuity on the $x-$axis, and α is a positive real number that controls the shape of the switching function (larger values cause a faster transition). Figure (7) shows a switching function for $y^- = 1$, $y^+ = 2$, and $x_d = 1$ for various values of α.

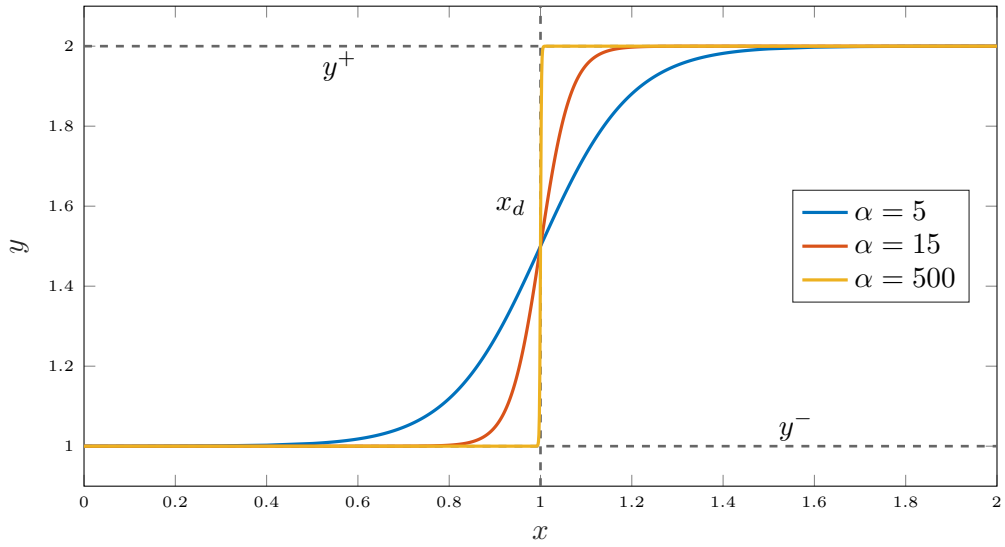

Figure 7. Switching function illustration

4.2.2 Computed Trajectories: Sequence One

This control sequence is computed by optimi-zing each time step independently of the others. The control sequence is plotted against the elapsed time in Figure (8), and the resulting angular velocity is also shown in Figure (8). The first obvious trend is that most of the torque magnitude is applied

about the x-axis. Since the inertia tensor is nearly diagonal, this is most likely related to the fact that the moment of inertia about that axis is the smallest, leading to the largest possible angular acceleration. Initially, the allowable torque is all applied about the x-axis, causing the angular velocity about that axis to quickly approach the 3 deg/s constraint. At 15 seconds elapsed time, the allowable torque is almost exclusively applied to the z-axis, then tapered down until the angular velocity about that axis approaches the allowed limit, around 45 seconds. At this point, the x-axis torque has tapered down to -1 Nm, and for the remaining duration the torque is mostly applied as something resembling a square wave about the x-axis. During this period, there is still some torque applied to the other two axes, mostly ranging between 0.1 and -0.2 Nm is y and 0.5 and -0.5 Nm in z, but these constitute a relatively small contribution to the applied torque.

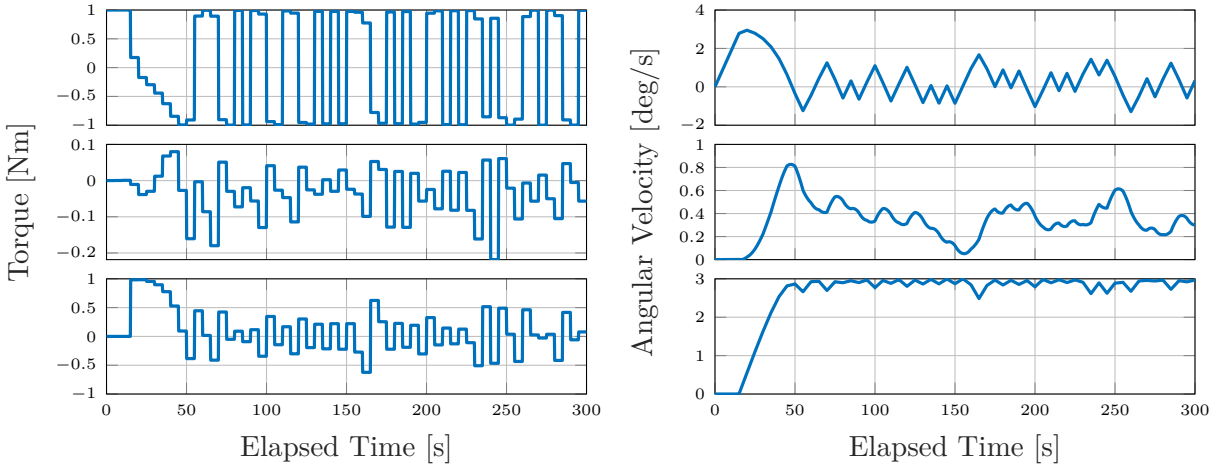

Figure 8. Control sequence and angular velocity with single step time horizon

4.2.3 Computed Trajectories: Sequence Two

The second control sequence is computed by optimizing the current time step along with the next step. This sequence along with the resulting angular velocity are shown in Figure (9). Perhaps unsurprisingly, this trajectory has much in common with the previous one: there is an initial concentration of torque about the x-axis, driving this component of the angular velocity toward the allowed maximum, followed by large torque about the z-axis driving that component of the angular velocity up; then, around 50 seconds elapsed, most of the control authority is applied as something like a square wave in along the x-axis. However, unlike the previous trajectory, the initial torque is in the negative x-direction, rather than the positive direction, and, the y-component of the angular velocity again has a peak around 45 seconds but in the negative direction this time.

4.2.4 Computed Trajectories: Sequence Three

The last trajectory is computed by optimi-zing three time steps at a time, and the computed control sequence and resulting angular velocity are displayed in Figure (10). Both the plots demonstrate similar behavior to the previous trajectory, computed with a two step horizon. One difference of note is that the range of the y-component of the angular velocity is less than the previous trajectory—around 0.6 rad/s instead of 1.0 rad/s.

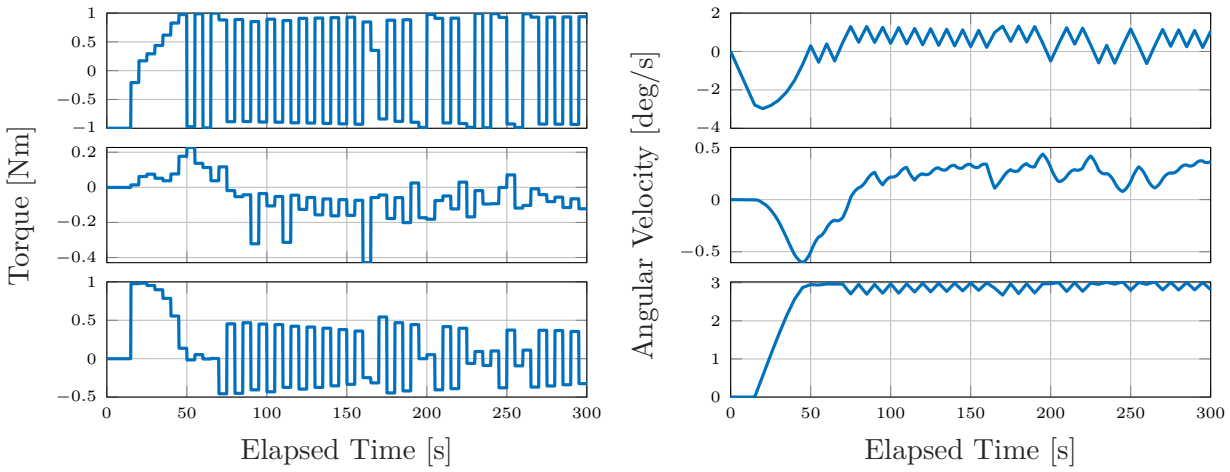

Figure 9. Control sequence and angular velocity with two step time horizon

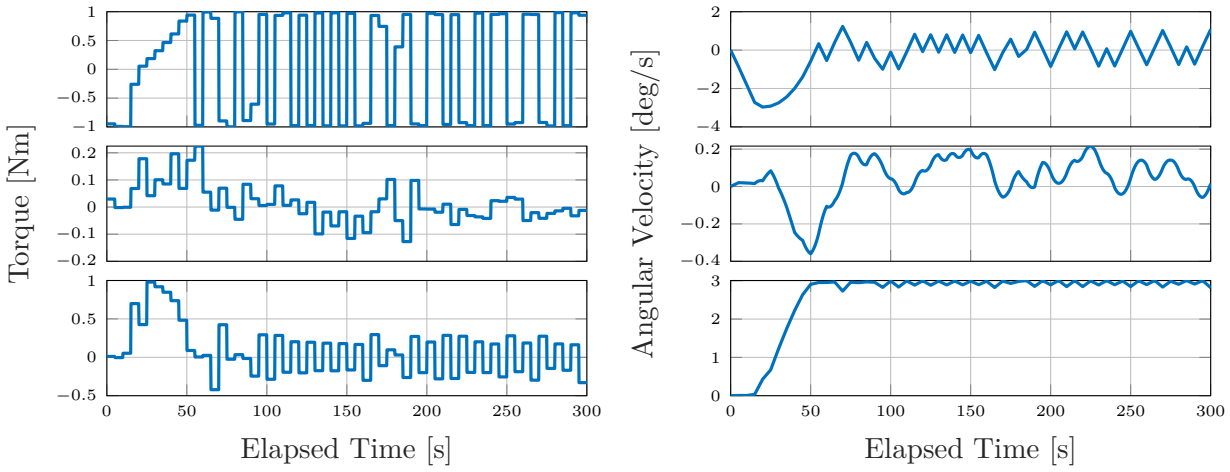

Figure 10. Control sequence and angular velocity with three step time horizon

4.2.5 Performance Comparison

An obvious way to compare the performance of each control sequence is to examine the cost function (the negative trace of the nonlinear observability Gramian) plotted against time; this is presented in Figure (11). The trend for each control sequence is so similar that, at the scale of Figure (11), it is impossible to see which sequence produces the lowest cost. This similarity seems intuitive, since the trajectories themselves share so many characteristics, but little can be concluded from this alone. Since the most important part of the figure is the end, a zoomed in view of the last ten seconds is included.

One would expect that more steps in the optimization time horizon would lead to a lower final cost, and this intuition holds for Sequence One which demonstrates the highest cost; however, contrary to this prediction, Sequence Two demonstrates slightly lower cost than Sequence Three. This discrepancy most likely indicates a trade off between the theoretical advantage of a larger time horizon and the increased numerical complexity that results from increasing the optimization space, since each additional time step increases the design space by 5 dimensions (three torque components and two constraints).

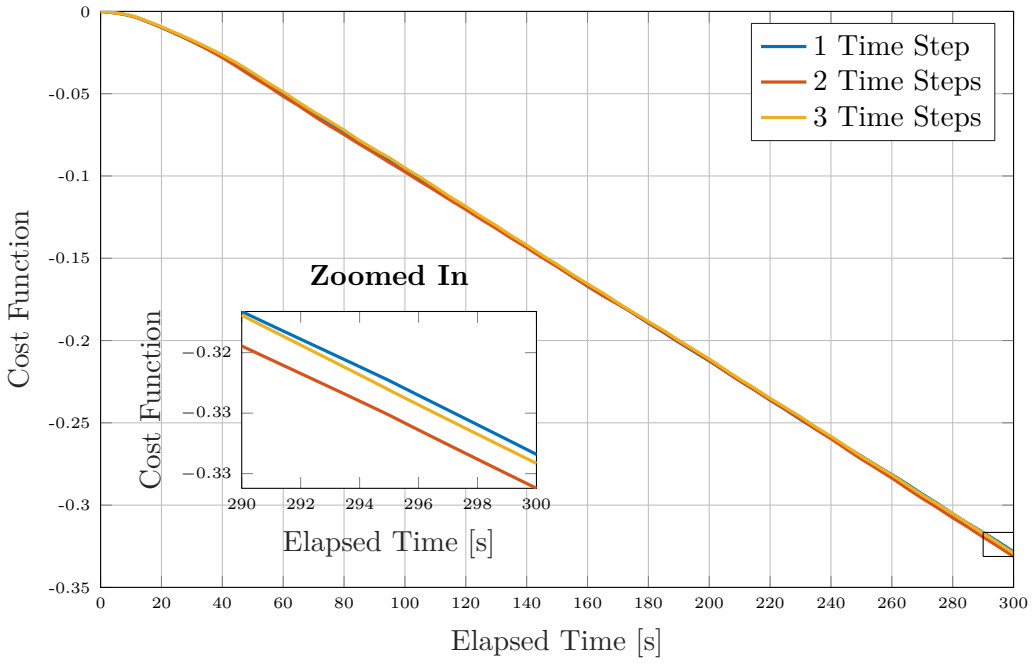

Figure 11. Cost function of each control sequence versus time

While the trace of the Gramian leads to a convenient cost function, it cannot, on its own, indicate if the Gramian is nonsingular, which is the theoretical condition for observability. To better assess the observability produced by each trajectory, the condition number of the matrix—the ratio of the largest eigenvalue to the smallest eigenvalue—is examined. The condition number can range from 1 to $+\infty$, where a smaller condition number indicates that the matrix inverse can be more accurately computed, and a larger condition number indicates that the matrix is closer to being singular. For each trajectory, the condition number of the observability Gramian computed along the optimized path is plotted against time, shown in Figure (12). Since the Gramian is initially singular, the condition number starts at $+\infty$, so the first 30 seconds are clipped off to allow more detail to be viewed. For all three control sequences, the condition number decreases exponentially for the first 40 seconds, at which point it begins to level out, and by this time, the condition for observability is met for each control sequence. Mirroring the trends in the cost function, Sequence Two clearly has the smallest condition number, followed by Sequence Three then Sequence One. Unlike the cost function, which is, by construction, non increasing in time, the condition number of each trajectory has a minimum prior to the final time. Initially, the smaller eigenvalues (which are more closely connected to inertia tensor observability) rapidly increase from zero, as the inertia tensor becomes observable through the system dynamics. This leads to the condition number plummeting from infinity toward a finite value. This effect is eventually outpaced by the growth of the large eigenvalues, related to angular velocity observability. These large eigenvalues increase at a faster rate than the small eigenvalues, since angular velocity is directly observed.

4.3 Inertia Tensor Estimation

To examine the performance of the developed estimators, the problem of estimating the inertia tensor of the James Webb Space Telescope (JWST) is considered. The inertia tensor and necessary reaction wheel parameters are listed in Table 1.

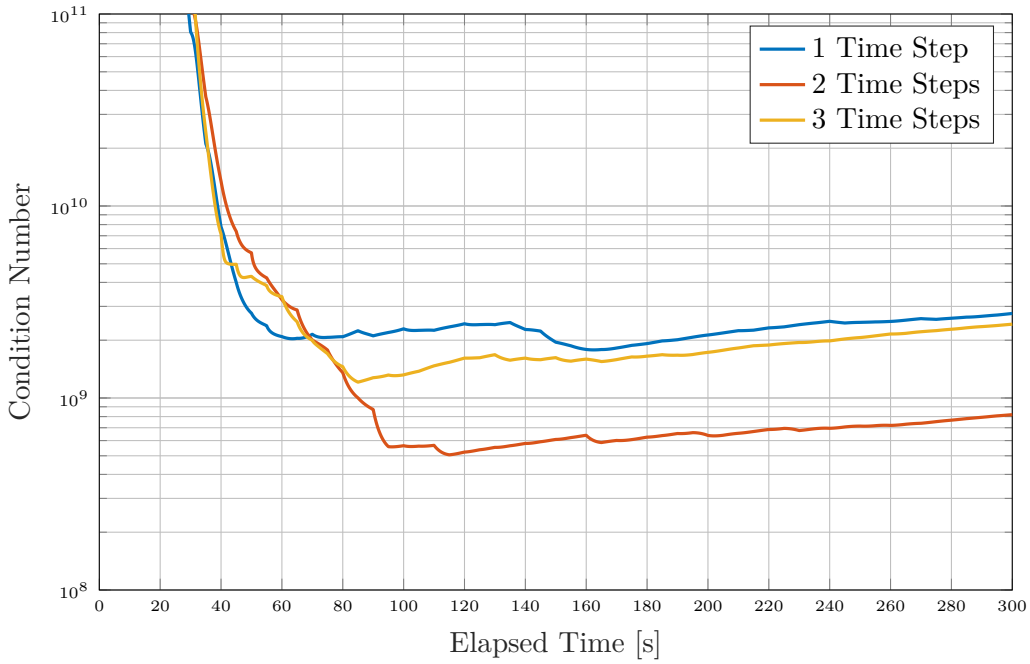

Figure 12. Gramian condition number of each control sequence versus time

Table 1. JWST Parameters [38]

Body frame inertia tensor	$\boldsymbol{J} = \begin{bmatrix} 67946 & -83 & 11129 \\ -83 & 90061 & 103 \\ 11129 & 103 & 45821 \end{bmatrix}$ kg · m^2
Wheel moment of inertia	$j_{\text{rw}} = 0.1295$ kg · m^2
Maximum wheel torque	$\tau_{\text{max}} = 0.072$ N · m
Slew momentum budget (per wheel)	30 N · m · s
Maximum wheel speed	6000 rpm
Wheel elevation angle	$\eta = 30°$

The reaction wheel alignment matrix for JWST is

$$\boldsymbol{G} = \begin{bmatrix} 0 & \frac{\sqrt{3}}{2}\cos(\eta) & \frac{\sqrt{3}}{2}\cos(\eta) & 0 & -\frac{\sqrt{3}}{2}\cos(\eta) & -\frac{\sqrt{3}}{2}\cos(\eta) \\ \cos(\eta) & \frac{1}{2}\cos(\eta) & -\frac{1}{2}\cos(\eta) & -\cos(\eta) & -\frac{1}{2}\cos(\eta) & 0.5\cos(\eta) \\ \sin(\eta) & \sin(\eta) & \sin(\eta) & \sin(\eta) & \sin(\eta) & \sin(\eta) \end{bmatrix} . \tag{102}$$

Reaction wheel torque commands are generated by

$$\boldsymbol{\tau}_a = \boldsymbol{G}^\dagger \boldsymbol{\tau}_d \, , \tag{103}$$

where $\boldsymbol{\tau}_d$ is the desired resultant torque and $\boldsymbol{G}^\dagger$ is the Moore-Penrose pseudoinverse of $\boldsymbol{G}$. The maximum resultant torque that can be generated about an arbitrary axis, $\boldsymbol{n}$, is limited by the maximum torque an individual wheel can apply,

$$\boldsymbol{\tau}_{a,\max} = \tau_{\max} \frac{\boldsymbol{G}^\dagger \boldsymbol{n}}{\|\boldsymbol{G}^\dagger \boldsymbol{n}\|} \, . \tag{104}$$

The spacecraft is assumed to exert the maximum reaction wheel torque about each body axis for 50 seconds in the positive direction, followed by 50 seconds in the negative direction, and repeats this sequence for a total elapsed time of 300 seconds.

Both gyro and star tracker measurements are processed by the filters. The gyro measurements are modeled based on the Northrop Grumman LN-200S[2], such that the standard deviation of the measurement noise is

$$\sigma_{g,v} = \frac{0.07^\circ}{\sqrt{\text{hr}}} \times \frac{\pi}{180^\circ} \times \frac{\sqrt{\text{hr}}}{60\sqrt{\text{s}}} \times \frac{1}{\sqrt{\Delta t_g}} \text{ rad/s} \ , \tag{105}$$

where $\Delta t_g = 0.01$ s is the sampling time of the gyroscope, and the initial standard deviation of the gyro bias is

$$\sigma_b = \frac{1^\circ}{\text{hr}} \times \frac{\pi}{180^\circ} \times \frac{\text{hr}}{3600\text{s}} \text{ rad/s} \, . \tag{106}$$

While gyro measurements are available at 100 Hz, measurements are processed in the filters at a downsampled rate of 1 Hz. The star tracker in this work is modeled after the Terma HE-5AS[3], so the standard deviation of the measurement noise is

$$\sigma_{st,v} = 5 \text{ arcsec} \times \frac{1^\circ}{3600 \text{ arcsec}} \times \frac{\pi}{180^\circ} \text{ rad} \, . \tag{107}$$

The initial true states are sampled from independent normal distributions. The attitude covariance is initially equal to the star tracker measurement noise covariance, and the angular velocity mean is zero and its initial covariance is the covariance of the gyro bias plus the gyro measurement noise covariance. The mean of the inertia tensor is taken to be the true inertia tensor of JWST, and two configurations for the inertia tensor uncertainty are considered. The first configuration is a "low" uncertainty scenario in which the standard deviation of each principal moment is 5% of the mean, and the attitude uncertainty for the principal axes is 1°, 1σ. The second configuration is a "high" uncertainty scenario in which the standard deviation of each principal moment is 15% of the mean, and the attitude uncertainty for the principal axes is 3°, 1σ.

[2]https://www.northropgrumman.com/wp-content/uploads/LN-200S-Inertial-Measurement-Unit-IMU-datasheet.pdf

[3]https://satsearch.co/products/terma-he-5as

Monte Carlo simulations with 1,000 trials are used to test the performance of the MEKF and the ICMEKF on both configurations of the initial uncertainty. On every Monte Carlo trial, the initial truth is sampled in accordance with the specifications previously detailed. If an impossible inertia tensor—one that violates any of the equality or inequality constraints required of a valid inertia tensor—is generated for the truth, that sample is discarded; it should be noted that this rarely occurs. The initial estimate and covariance for the filter, whether it be the MEKF or ICMEKF, is held fixed across the trials. Gyro and star tracker measurements are processed by each filter at 1 Hz, where the measurement noises are sampled according to their statistics at each measurement return and across each Monte Carlo trial.

Monte Carlo simulations with 500 trials are used to test the performance of the GPFF and BSGPFF on the "high" uncertainty scenario. Both particle filter variants are implements with 250 particles. Compared to a more traditional particle filter, this is a small number of particles, but the ability to use a small number of particles is an attractive property of the particle flow filters. Even so, the computational complexity of the GPFF and BSGPFF is higher than that of the MEKF and ICMEKF, which is why fewer Monte Carlo simulations are considered.

4.3.1 Low Uncertainty

The low uncertainty configuration—which is represented by 5% (1σ) initial uncertainty in each principal moment and 1° (1σ) initial uncertainty in each principal axis—is considered first. This configuration is intended as a baseline performance case in which the initial uncertainties are not "too large," such that both the MEKF and ICMEKF should perform similarly. The results for the MEKF are presented in Figures (13) and (14), and the results for the ICMEKF are presented in Figures (15) and (16).

Note that each set of plots within each figure contains four curves: 1) the blue line represents the estimation error of a single trial from the Monte Carlo simulation; 2) the orange line represents the $\pm 3\sigma$ uncertainty interval of the same single trial; 3) the dashed gray line represents the average estimation error across all 1,000 trials; and 4) the dashed black line represents the $\pm 3\sigma$ uncertainty interval determined from the sample statistics across all 1,000 trials.

There are a few hallmarks of a well-behaved estimator: a) the average estimation error should be close to zero; b) the $\pm 3\sigma$ interval from a single trial should closely resemble the $\pm 3\sigma$ obtained from the sample statistics; and c) the single-trial estimation error should largely remain within the $\pm 3\sigma$ interval. Concerning a), the estimator is said to be unbiased whenever the average estimation error is near-zero. Concerning b), the estimator is deemed conservative whenever the single-trial $\pm 3\sigma$ interval encloses the $\pm 3\sigma$ interval from the sample statistics, and the estimator is deemed over-confident when the opposite situation occurs; likewise, when the $\pm 3\sigma$ intervals align with one another, the estimator is said to be statistically consistent.

For the MEKF, the attitude and angular velocity estimation performance are summarized in Figure (13), and the the principal axes and principal moments estimation performance are summarized in Figure (14). Each of these figures demonstrates that the MEKF is largely unbiased, save for a few departures from near-zero average estimation error near the beginning of the simulation. These are instances in which the filter is processing information and rapidly decreasing the uncertainty, such that transient behaviors are acceptable. The MEKF results also demonstrate that the filter is relatively statistically consistent, with slightly conservative behavior that arises near the end of the simulation interval.

The results of the ICMEKF are summarized in Figure (15) for the attitude and angular velocity states and in Figure (16) for the principal axis and principal moment states. The filter performance in Figures (15) and (16) is strikingly similar to that of Figures (13) and (14). This occurs because

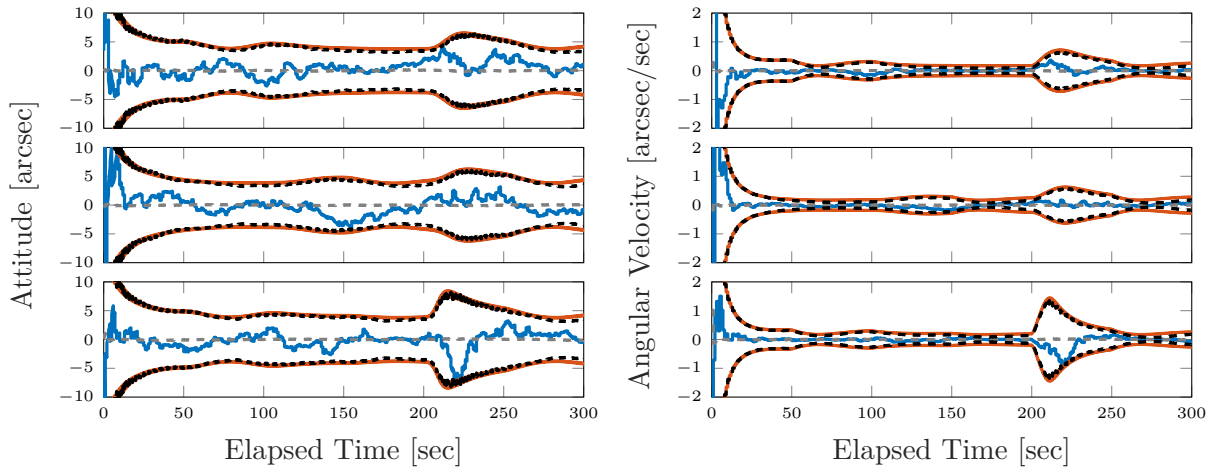

Figure 13. Attitude (left) and angular velocity (right) estimation error for Scenario #1 with the MEKF

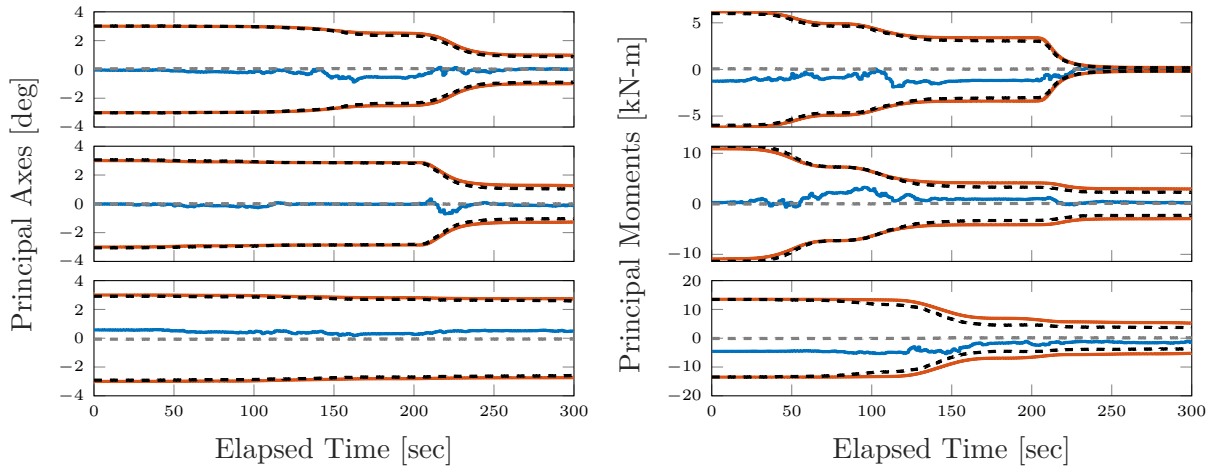

Figure 14. Principal axis (left) and moments (right) estimation error for Scenario #1 with the MEKF

of the size of the initial uncertainty. There are no instances for this low uncertainty case in which the MEKF produces an inertia tensor that violates the constraints; as such, the ICMEKF does not have to deal with the inequality constraints and resorts to performance directly in line with that of the MEKF. That is, the ICMEKF is observed to be unbiased, except for initial transients, and it is observed to be statistically consistent, except for conservative performance near the end of the simulation interval.

4.3.2 High Uncertainty

Now, the high uncertainty configuration—which is represented by 15% (1σ) initial uncertainty in each principal moment and 3° (1σ) initial uncertainty in each principal axis—is examined. This scenario is intended as an edge case where the initial uncertainties are "large enough" to push the capabilities of the MEKF and illustrate differences between the MEKF and the proposed ICMEKF.

The performance of the MEKF for attitude and angular velocity estimation is summarized in

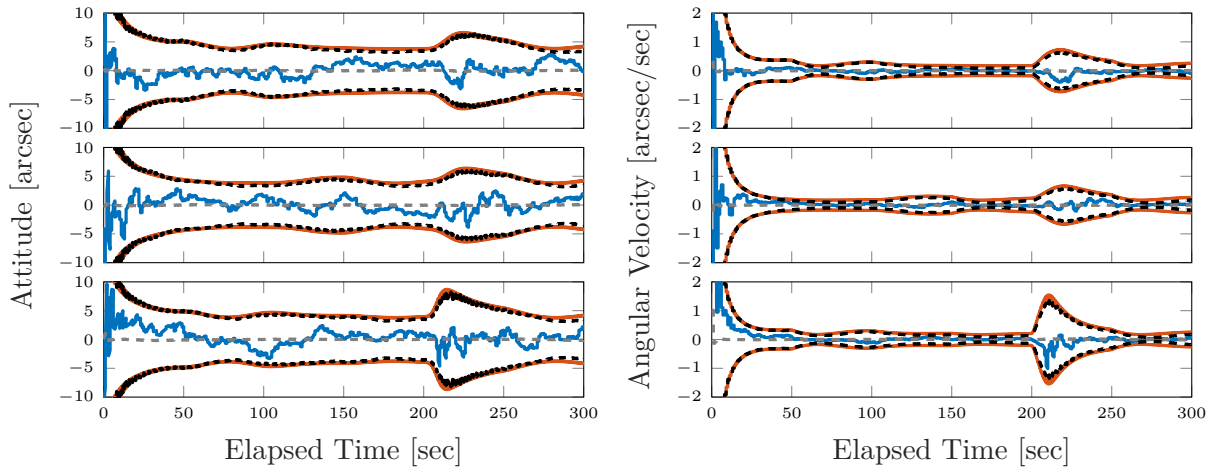

Figure 15. Attitude (left) and angular velocity (right) estimation error for Scenario #1 with the ICMEKF

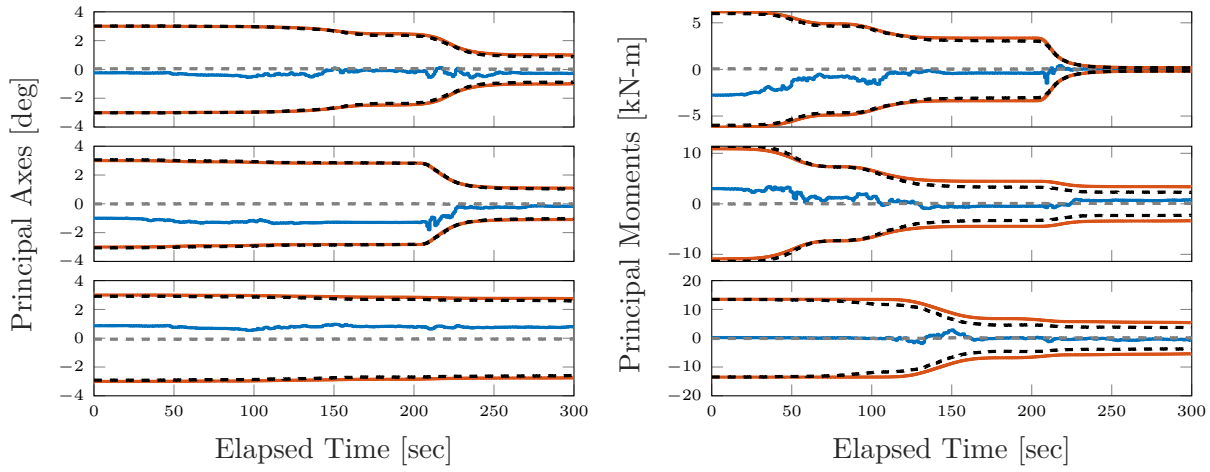

Figure 16. Principal axis (left) and moments (right) estimation error for Scenario #1 with the ICMEKF

Figure (17). Likewise, the performance of the MEKF for principal axes and principal moments estimation is summarized in Figure (18). Much like the scenario considered in Section 4.3.1, the results illustrated in Figure (17) convey that the MEKF is unbiased and statistically consistent in the estimation of the attitude and angular velocity states. This is not surprising, as these states are directly related to the measurements. The situation becomes more interesting when looking at the results illustrated in Figure (18). Figure (18) indicates that the MEKF remains unbiased, but over-confident behavior is observed in two of the three channels of the principal axes states. Estimation of the principal moments, on the other hand, remains relatively well-behaved throughout the duration of the simulation.

Performance summaries for the ICMEKF are given in Figure (19) for the attitude and angular velocity stated and in Figure (20) for the principal axis and principal moment states. As with the MEKF, the attitude and angular velocity performance illustrated in Figure (19) demonstrate both unbiased and statistically consistent estimation. Again, this is not an unexpected outcome,

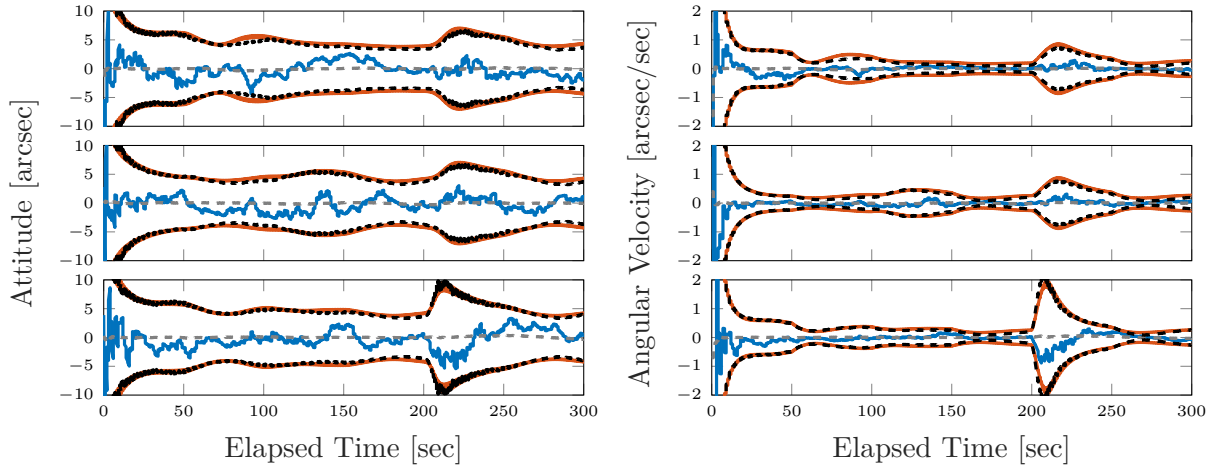

Figure 17. Attitude (left) and angular velocity (right) estimation error for Scenario #2 with the MEKF

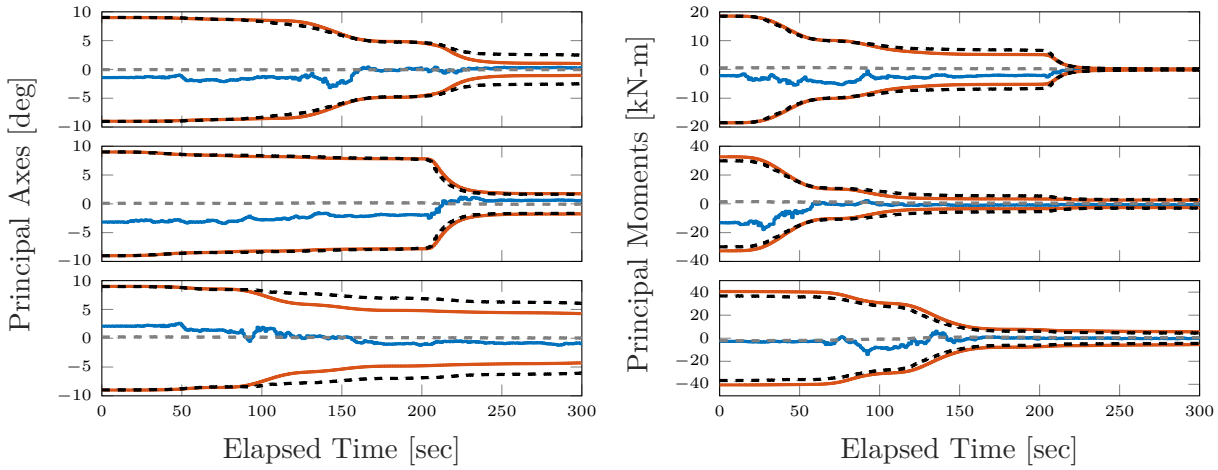

Figure 18. Principal axis (left) and moments (right) estimation error for Scenario #2 with the MEKF

given that these states are directly related to the measurements. Unlike the scenario considered in Section 4.3.1, however, the performance of the ICMEKF in estimating the principal axis and principal moments states varies significantly from that of the MEKF. Regarding the estimation of the principal axis states, the ICMEKF is observed to be more conservative than the MEKF in two channels and over-confident in one of the channels. Direct comparison of Figure (20) with Figure (18) indicates that the ICMEKF is, overall, doing a better job of representing the uncertainty trends, especially in the third channel of the principal axis states. Estimation of the principal moments states, on the other hand, is largely comparable between the ICMEKF and the MEKF, with both filters remaining relatively well-behaved throughout the duration of the simulation.

Up to this point, the analysis has focused on the estimation performance achieved by the MEKF and the ICMEKF. Both the MEKF and ICMEKF handle the equality constraints associated with the attitude states in the same way. The inequality constraints on the principal moments, however, are treated differently by the two filters. The MEKF does not take into account these constraints at

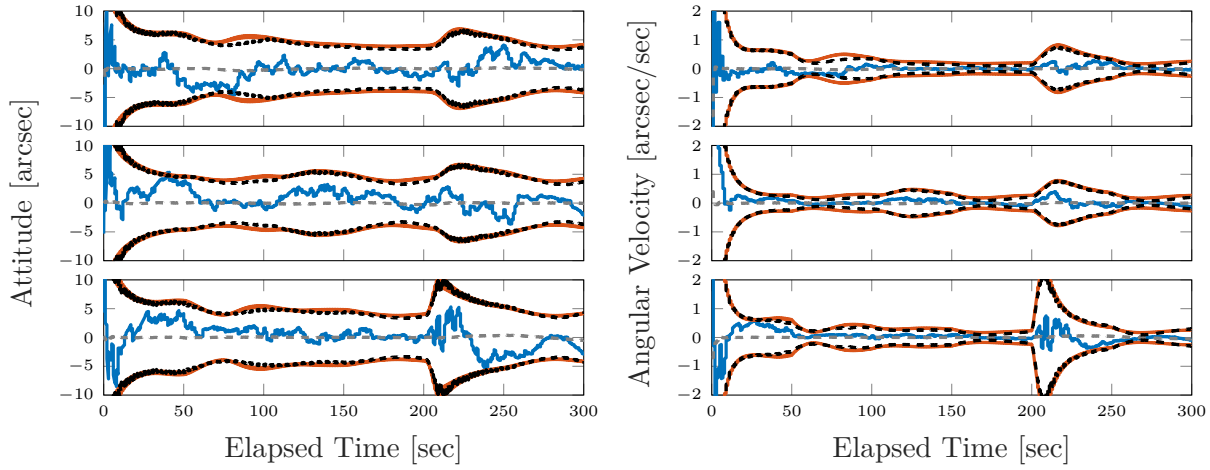

Figure 19. Attitude (left) and angular velocity (right) estimation error for Scenario #2 with the ICMEKF

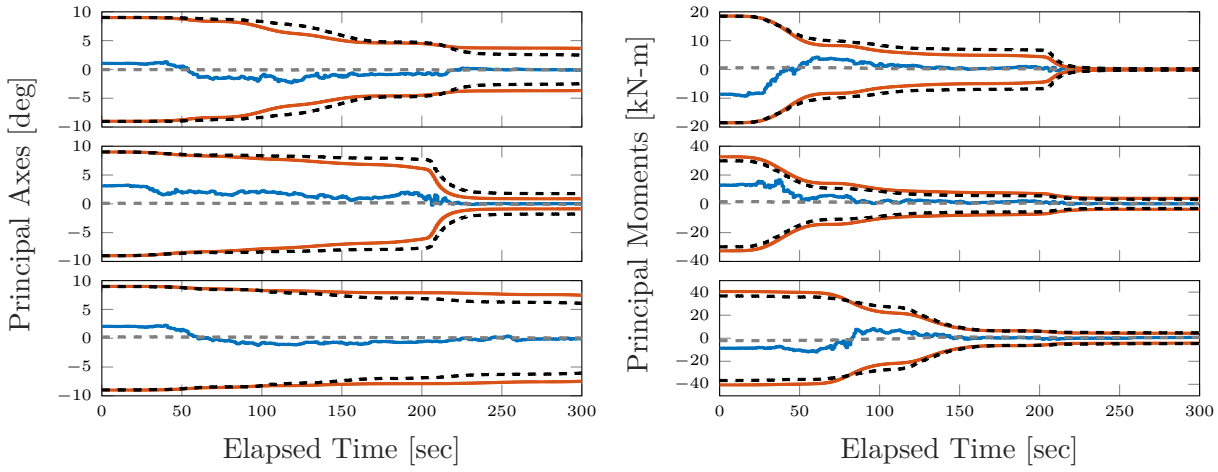

Figure 20. Principal axis (left) and moments (right) estimation error for Scenario #2 with the ICMEKF

all, whereas the ICMEKF is formulated as a quadratic programming problem with linear inequality constraints. As the uncertainties in the initial understanding of the inertia properties increases, it becomes more difficult to guarantee that constraints are satisfied.

As a reminder, the inequality constraints are comprised of three triangle inequality constraints and three positivity constraints. At each point in time, the estimates produced by the MEKF and the ICMEKF are tested for constraint satisfaction. If the triangle inequality is not satisfied, this is recorded as an invalid estimate, and if the principal moments are not positive, this is recorded separately as an invalid estimate. This process is carried out for all 1,000 Monte Carlo trials, and the results are presented in Figure (21). The orange curves in Figure (21) represent the number of invalid inertia tensor estimates recorded based on the triangle inequality constraints, and the blue curves in Figure (21) represent the number of invalid inertia tensor estimates recorded based on the positivity constraints. It is clear that the triangle inequality is the dominant—in fact, the only—source of invalid inertia tensor estimates. The MEKF reaches a peak of 18 trials out of 1,000

producing invalid estimates. The ICMEKF reaches a peak of 1 trial out of 1,000 producing invalid estimates. This is clearly a vast improvement on the MEKF invalid estimate rate, but it is curious since the constraints are built into the optimization process. The remaining instances of constraint violations are believed to be due to numerical considerations and the tolerances specified in solving the optimization problem.

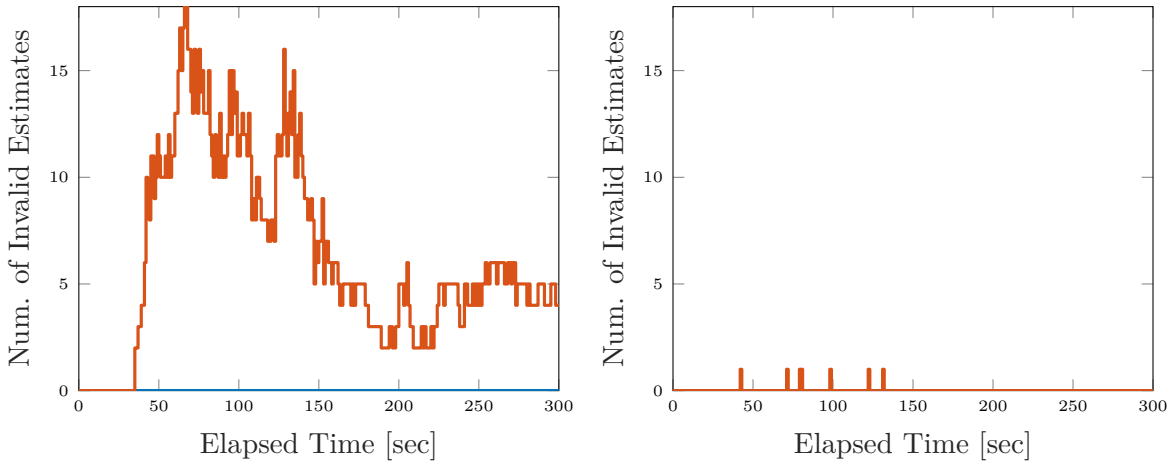

Figure 21. Instantaneous invalid estimates for the MEKF (left) and ICMEKF (right) for Scenario #2

The data presented in Figure (21) is further processed to determine how many unique trials out of the set of 1,000 have an instance where the filter produces an invalid inertia tensor estimate. Once the filter produces an invalid estimate, the trial is considered to have failed. This is determined for both the MEKF and for the ICMEKF. The trends of failed trials as a function of time for the MEKF and ICMEKF are illustrated in Figure (22). The MEKF has 74 trials that fail, whereas the ICMEKF has only 7. Thus, while there is still room for improvement, the ICMEKF is a 10-fold improvement over the MEKF in terms of producing valid inertia tensor estimates.

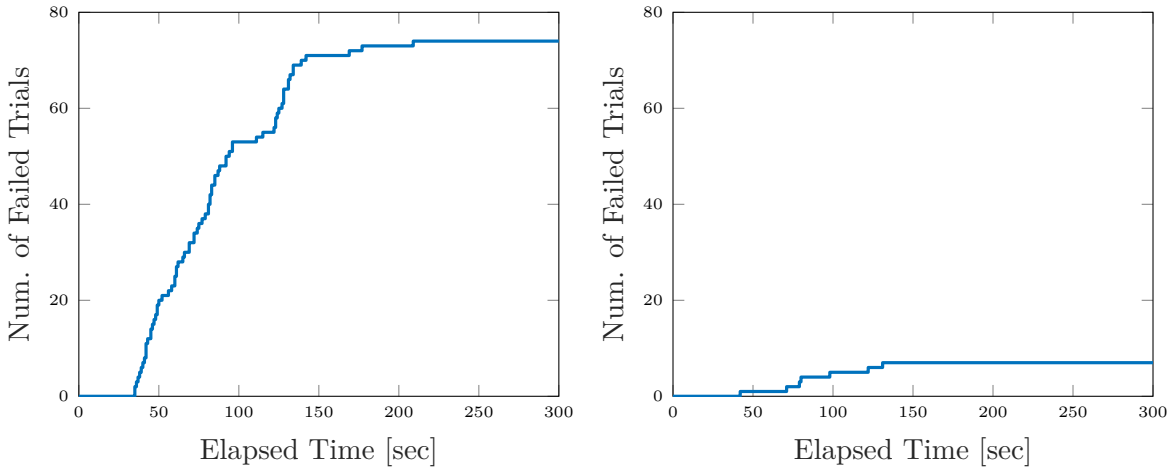

Figure 22. Cumulative failures for the MEKF (left) and ICMEKF (right) for Scenario #2

The GPFF and BSGPFF approaches are also tested under the conditions of Scenario #2, in

order to assess the performance of a higher order approach. Both filters are implemented with 250 particles—far fewer than is usually required for particle filter implementations. Still, these estimators are more computationally expensive than the MEKF, so only 500 Monte Carlo trials are performed. The estimation performance for the inertia parameters is recorded in Figure (23) for the GPFF and in Figure (24) for the BSGPFF. Both filters appear to be unbiased, and they show similar performance in their estimation of the principal axes, with some overconfidence in all channels. Both filters appear to do a good job of quantifying the uncertainty in their estimates of the principal axes, especially by the end of the simulation. The BSGPFF shows some overconfidence in the third principal moment estimate around 100 seconds elapsed time; however, this is corrected by the midpoint of the simulation. This may be an artifact of the particles that have stuck to the constraint boundary pulling the mean of the particles toward the boundary while having a relatively small spread that leads to a smaller covariance. This could only happen in the principal moment states, since these are the ones constrained by inequality relationships.

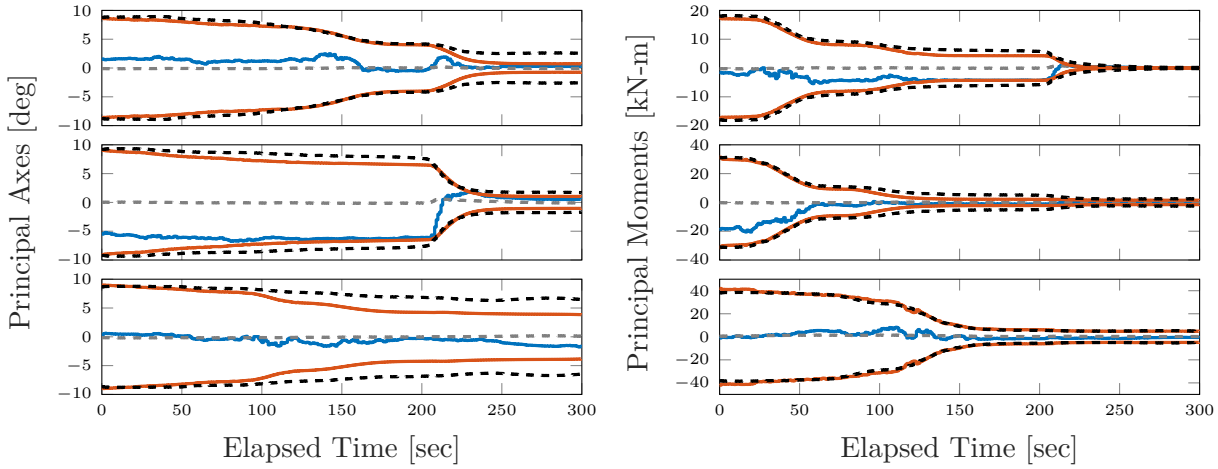

Figure 23. Principal axis (left) and moments (right) estimation error for Scenario #2 with the GPFF

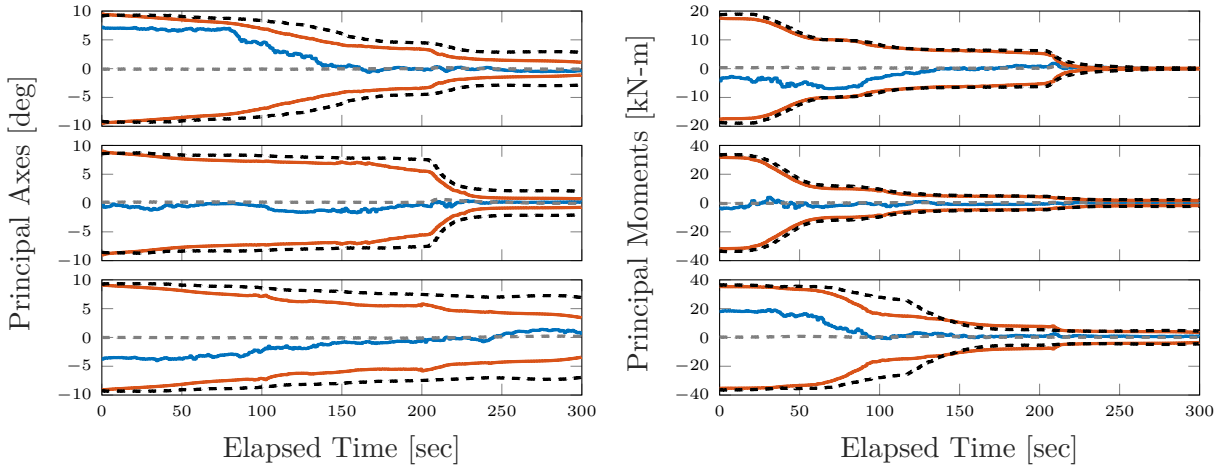

Figure 24. Principal axis (left) and moments (right) estimation error for Scenario #2 with the BSGPFF

It should be noted that a run of the GPFF is considered a failure if, at any point in time, 225 of the 250 particles (or 90%) are in violation of the constraints. This did happen one time, so this trial is excluded from the computation of the Monte Carlo statistics in order to not skew the results with an outlier. Recall that the BSGPFF is implemented such that particles cannot be in violation of the constraints. These two filter implementations represent a tradeoff, then, between ability to accurately represent the conditional PDF and robustness. That being said, both filters would very likely demonstrate improved self consistency with more particles, since 250 is extremely few for a system of such large dimension, even for particle flow filters.

5.0 CONCLUSIONS

Timely, accurate, and precise estimation of spacecraft mass properties, such as the inertia tensor, using onboard measurement data is key to enabling precision attitude control and understanding the configuration of a vehicle on-orbit. Estimating the inertia tensor, however, is complicated by the constraints required to produce a valid representation of the mass distribution. Three aspects of the inertia tensor estimation process are considered in this work: 1) selection of the parameters to estimate, 2) determination of proper control input signals, and 3) adhering to constraints in the estimation process.

Proper coordinate selection impacts observability and estimation performance. For the inertia tensor, there are two viable candidates: moments and products of inertia in a body-fixed coordinate system or the principal moments of inertia and the attitude of the principal axis coordinate system. Working with principal moments and axes is found to simplify the constraint structure required to be imposed to obtain valid inertia tensor estimates and is therefore the parameterization selected for the observability and estimation methods developed in this work.

Observability analysis can be carried out in a number of ways in order to assess the influence of different control signals. In this work, both linearized and nonlinear observability analysis are investigated. A method for computing a sequence of control torques to maximize the observability of a rigid body system is developed and analyzed. Control sequences are computed by maximizing the trace of the Gramian formed by the nonlinear observability matrix at the fixed final time, subject to constraints on the magnitude of the torque and on the magnitude of the spacecraft angular velocity. Control torques are computed with a moving time horizon, and three different time horizons (one, two, and three time steps) are investigated. Control sequences are analyzed by examining the cost function and the condition number of the observability Gramian. While all of the control sequences produces inertia tensor observability, the control sequence computed with a moving time horizon of two steps yields the best results. This demonstrates a tradeoff between the theoretical benefits of a longer time horizon and the computational complexity of increasing the design space with more steps computed simultaneously.

Conventional estimation techniques, such as the extended Kalman filter (EKF), are incapable of enforcing constraints on the estimated parameters. This work proposes, develops, and analyzes a constrained estimator based on a reformulation of the approximate linear minimum mean-square error framework. This gives rise to a variant of the EKF. Quadratic equality constraints related to attitude parameterizations are handled through the multiplicative EKF (MEKF), and linear inequality constraints are handled through a constrained quadratic programming problem, leading to an inequality constrained MEKF (ICMEKF). Additionally, approximate Bayesian methods are also developed based on the concept of particle flow filters, where constraints are naturally handled through manipulation of the particles. Two methods for handling the constraints are developed, leading to the Gaussian particle flow filter (GPFF) and the boundary-sticking GPFF (BSGPFF).

The proposed ICMEKF, GPFF, and BSGPFF methods are applied to the problem of estimating the inertia tensor during a calibration maneuver sequence. It is observed that the proposed ICMEKF method achieves similar performance to an unconstrained estimator for a case of relatively low initial uncertainty. When higher levels of uncertainty are considered, however, the proposed ICMEKF method produces estimates that are invalid ten times less often than existing methods while remaining unbiased and reasonably statistically consistent. Even with large initial inertia tensor uncertainty, the GPFF and BGSPFF methods are both able to produce unbiased estimates that satisfy the constraints of the inertia tensor and quantify the uncertainty reasonably well, even with few particles. The GPFF implementation does record one trial in which too many particles violate the constraint, and the BSGPFF implementation displays a slightly worse ability to quantify the inertia uncertainty compared to the GPFF, indicating a tradeoff in these approaches between robustness and accuracy. Nevertheless, both of these approaches demonstrate good performance, and they would likely produce better covariance estimates with additional particles.

REFERENCES

[1] Norman, M. C., Peck, M. A., and O'Shaughnessy, D. J., "In-Orbit Estimation of Inertia and Momentum-Actuator Alignment Parameters," *Journal of Guidance, Control, and Dynamics*, Vol. **34**, No. 6, 2011, pp. 1798–1814.

[2] Manchester, Z. R. and Peck, M. A., "Recursive Inertia Estimation with Semidefinite Programming," *AIAA Guidance, Navigation, and Control Conference*, 2017.

[3] Tanygin, S. and Williams, T., "Mass Property Estimation Using Coasting Maneuvers," *Journal of Guidance, Control, and Dynamics*, Vol. **20**, No. 4, 1997, pp. 625–632.

[4] Psiaki, M. L., "Estimation of a Spacecraft's Attitude Dynamics Parameters by Using Flight Data," *Journal of Guidance, Control, and Dynamics*, Vol. **28**, No. 4, 2005, pp. 594–603.

[5] Bergmann, E. V., Walker, B. K., and Levy, D. R., "Mass property estimation for control of asymmetrical satellites," *Journal of Guidance, Control, and Dynamics*, Vol. **10**, No. 5, 1987, pp. 483–491.

[6] Nuthi, P. and Subbarao, K., "Computational Adaptive Optimal Control of Spacecraft Attitude Dynamics with Inertia-Matrix Identification," *Journal of Guidance, Control, and Dynamics*, Vol. **40**, No. 5, 2017, pp. 1257–1261.

[7] Ahmed, J., Coppola, V. T., and Bernstein, D. S., "Adaptive Asymptotic Tracking of Spacecraft Attitude Motion with Inertia Matrix Identification," *Journal of Guidance, Control, and Dynamics*, Vol. **21**, No. 5, 1998, pp. 684–691.

[8] Kim, D. H., Yang, S., Cheon, D.-I., Lee, S., and Oh, H.-S., "Combined estimation method for inertia properties of STSAT-3," *Journal of Mechanical Science and Technology*, Vol. **24**, No. 8, 2010, pp. 1737–1741.

[9] Helmuth, J. C., Darling, J. E., and DeMars, K. J., "Recursive Multiplicative Estimation of Rigid Body Attitude and Moment of Inertia," *AAS/AIAA Space Flight Mechanics Meeting*, No. AAS 19-429, 2019.

[10] Kailath, T., *Linear Systems*, Prentice-Hall, Inc, 1980.

[11] Helmuth, J. C. and DeMars, K. J., "Observability Study for Estimation of Rigid Body Attitude and Inertia Tensor," *AIAA SciTech Forum*, Orlando, FL, 2020.

[12] Powel, N. D. and Morgansen, K. A., "Empirical observability Gramian rank condition for weak observability of nonlinear systems with control," *2015 54th IEEE Conference on Decision and Control (CDC)*, 2015, pp. 6342–6348.

[13] Zimmer, S. J., *Reducing Spacecraft State Uncertainty Through Indirect Trajectory Optimization*, Ph.D. thesis, The University of Texas, Austin, TX, December 2005.

[14] Hermann, R. and Krener, A., "Nonlinear controllability and observability," *IEEE Transactions on Automatic Control*, Vol. **22**, No. 5, 1977, pp. 728–740.

[15] Huxel, P. J., *Navigation Algorithms and Observability Analysis for Formation Flying Missions*, Ph.D. thesis, The University of Texas, Austin, TX, May 2006.

[16] Gelb, A., *Applied Optimal Estimation*, The M.I.T. Press, 1974.

[17] Kalman, R. E., "A New Approach to Linear Filtering and Prediction Problems," *Transactions of the ASME–Journal of Basic Engineering*, Vol. **82**, No. Series D, 1960, pp. 35–45.

[18] Crassidis, J. L., Markley, F. L., and Cheng, Y., "Survey of Nonlinear Attitude Estimation Methods," *Journal of Guidance, Control, and Dynamics*, Vol. **30**, No. 1, 2007, pp. 12–28.

[19] Richards, P., "Constrained Kalman Filtering Using Pseudo-measurements," *IEE Colloquium on Algorithms for Target Tracking*, 1995, pp. 75–79.

[20] Lawson, C. L. and Hanson, R. J., *Solving Least Squares Problems*, chap. 20–22, Society for Industrial and Applied Mathematics, Philadelphia, PA, 1995.

[21] Simon, D. and Chia, T. L., "Kalman filtering with state equality constraints," *IEEE Transactions on Aerospace and Electronic Systems*, Vol. **38**, No. 1, 2002, pp. 128–136.

[22] Lawson, C. L. and Hanson, R. J., *Solving Least Squares Problems*, chap. 23, Society for Industrial and Applied Mathematics, Philadelphia, PA, 1995.

[23] Simon, D. and Simon, D. L., "Kalman Filtering with Inequality Constraints for Turbofan Engine Health Estimation," Tech. rep., National Aeronautics andSpace Administration, February 2003.

[24] Shuster, M. D., "A Survey of Attitude Representations," *The Journal of the Astronautical Sciences*, Vol. **41**, No. 4, 1993, pp. 439–517.

[25] Markley, F. L. and Crassidis, J. L., *Fundamentals of Spacecraft Attitude Determination and Control*, Springer, 2014.

[26] Peck, M. A., "Uncertainty Models for Physically Realizable Inertia Dyadics," *Journal of the Astronautical Sciences*, Vol. **54**, March 2006, pp. 1–16.

[27] Anguelova, M., *Observability and identifiability of nonlinear systems with applications in biology*, Ph.D. thesis, Chalmers University of Technology and Gothenburg University, Gothenburg, Sweden, 2007.

[28] Yu, Z., Cui, P., and Zhu, S., "Observability-Based Beacon Configuration Optimization for Mars Entry Navigation," *Journal of Guidance, Control, and Dynamics*, Vol. **38**, No. 4, 2015, pp. 643–650.

[29] Skelton, R. E., *Dynamic Systems Control: Linear Systems Analysis and Synthesis*, John Wiley and Sons, 1988, pp. 25–26.

[30] Krener, A. J. and Ide, K., "Measures of unobservability," *Proceedings of the 48h IEEE Conference on Decision and Control (CDC) held jointly with 2009 28th Chinese Control Conference*, 2009, pp. 6401–6406.

[31] Zanetti, R. and DeMars, K. J., "Fully Multiplicative Unscented Kalman Filter for Attitude Estimation," *Journal of Guidance, Control, and Dynamics*, Vol. **41**, No. 5, 2018, pp. 1181–1187.

[32] Dhrymes, P. J., *Mathematics for Econometrics*, Springer, 4th ed., 2013.

[33] Zellner, A., "Optimal Information Processing and Bayes's Theorem," *The American Statistician*, Vol. **42**, No. 4, November 1988, pp. 278–280.

[34] Ward, K. C., *Information-Based Methods and Models for Particle Flow Filtering*, Ph.D. thesis, Missouri University of Science and Technology, Rolla, MO, 2021.

[35] Daum, F., Huang, J., and Noushin, A., "Exact particle flow for nonlinear filters," *Signal Processing, Sensor Fusion, and Target Recognition XIX*, edited by I. Kadar, Vol. 7697, International Society for Optics and Photonics, SPIE, 2010, pp. 92 – 110.

[36] Ward, K. C. and DeMars, K. J., "A Square-Root Factorized Multiplicative Extension to the Particle Flow Filter," *2020 Astrodynamics Specialist Conference*, No. AAS 20-633, 2020.

[37] Markley, F. L., Cheng, Y., Crassidis, J. L., and Oshman, Y., "Averaging Quaternions," *Journal of Guidance, Control, and Dynamics*, Vol. **30**, No. 4, 2007, pp. 1193–1197.

[38] Karpenko, M., King, J. T., Dennehy, C. J., and Michael Ross, I., "Agility Analysis of the James Webb Space Telescope," *Journal of Guidance, Control, and Dynamics*, Vol. **42**, No. 4, 2019, pp. 810–821.

LIST OF SYMBOLS, ABBREVIATIONS, AND ACRONYMS

BSGPFF	Boundary-Sticking Gaussian Particle Flow Filter
CAD	Computer Aided Design
DCM	Direction Cosine Matrix
EKF	Extended Kalman Filter
GPFF	Gaussian Particle Flow Filter
ICMEKF	Inequality-Constrained Multiplicative Extended Kalman Filter
IMU	Inertial Measurement Unit
MEKF	Multiplicative Extended Kalman Filter
ODE	Ordinary Differential Equation
PDF	Probability Density Function

DISTRIBUTION LIST

DTIC/OCP 8725 John J. Kingman Rd, Suite 0944 Ft Belvoir, VA 22060-6218	1 cy
AFRL/RVIL Kirtland AFB, NM 87117-5776	1 cy
Official Record Copy AFRL/RVS/David King	1 cy

(This Page Intentionally Left Blank)